UNIVERSIDAD DE CONCEPCIÓN
DIRECCIÓN DE POSTGRADO
FACULTAD DE CIENCIAS FÍSICAS Y MATEMÁTICAS

FORMATION OF SMBH SEEDS IN POP III STAR CLUSTERS THROUGH COLLISIONS : THE IMPORTANCE OF MASS LOSS

Por: Patricio Javier Alister Seguel

Tesis presentada a la Facultad de Ciencias Físicas y Matemáticas de la Univerisdad de Concepción para optar al grado académico de Magister en Astronomía.

Junio 2020
Concepción, Chile

Profesor Guía: Dr. Dominik Schleicher

Agradecimientos

Me gustaría agradecer a la familia Alister Seguel, particularmente mis papás Jessica y Patricio, por haberme criado y mantenido, y darme un pilar fundamental para crecer haciendo las cosas que me gustan.

I would also like to acknowledge my professor and supervisor Dominik Schleicher who guided me in an insighful way trough all my thesis process, taught me a lot during the last years and with whom I have had good moments and beers. I also wanted to acknowledge my collaborators Michael Fellhauer, Ralf Klessen and Tjarda Boekholt for their always useful advice and corrections.

También quiero agradecer especialmente a mis compañeros de la carrera de astronomía, que hicieron que el camino fuera siempre mucho más facil y ameno, y a mis amigos con quienes compartí todo lo que pude sobre mi trabajo y me apoyaron siempre.

Finally I want to thanks for the support via Fondecyt regular 1161247 and Conicyt PIA ACT172033.

Resumen

En este trabajo mostramos la importancia de calcular la pérdida de masa en colisiones estelares, en el contexto de formación de semillas de agujeros negros supermasivos, en cúmulos estelares densos primordiales de Población III. El proceso de creación de la semilla puede ser acentuado por la acreción, como modelos recientes de formacion de semillas de agujeros negros en cúmulos de Población III han mostrado. Esto podría explicar la presencia de agujeros negros supermasivos a alto redshift, $z > 6$. Sin embargo, en este contexto, la pérdida de masa durante colisiones no ha sido considerado y podría jugar un rol importante en la formación de la semilla. Estudiamos el efecto de la pérdida de masa, debido a colisiones de protoestrellas, en la formación y evolución de un objeto masivo en un cúmulo primordial denso, usando el código AMUSE. Consideramos tanto perdidas de masa constante por colisión como también modelos analíticos basados en la estructura estelar de los componentes de la colisión, en 6 modelos de acreción distintos. En escenarios con pérdida de masa constante por colisión variamos el porcentaje de masa perdida por colisión en cada simulación, y realizamos 5 simulaciones por cada caso y por cada modelo de acreción, y también cuando usamos modelos analíticos. Nuestros cálculos indican que la pérdida de masa puede afectar significativamente la masa final de la posible semilla de agujero negro. Considerando una pérdida de masa constante del 5 % por cada colisión, es posible perder entre 60-80% de la masa total obtenida al no considerar pérdida de masa. Si usamos ahora los modelos analíticos para la pérdida de masa, la masa del objeto central final es reducida entre 15-40%, dependiendo el modelo de acreción que consideremos. En total, obtenemos masas finales del orden de $10^4 M_\odot$, que sigue siendo suficiente masivo para ser una semilla de agujero negro supermasivo, mostrando que el modelo de colisiones en cúmulos primordiales es exitoso explicando la formación de estos objetos, aún si se considera la pérdida de masa.

Keywords – Población III, agujeros negros, pérdida de masa

Abstract

In this work we show the importance of mass loss calculations when considering the formation of supermassive black hole (SMBH) seeds, in runaway collision scenarios in dense Population III primordial clusters. The seed creation process can be further enhanced by accretion, as recent models of SMBH seed formation in Population III star clusters have shown. This may explain the presence of supermassive black holes already at high redshift, $z > 6$. However, in this context, mass loss during collisions has not been considered and could play an important role for the formation of the SMBH seed. We study the effect of mass loss, due to collisions of protostars, in the formation and evolution of a massive object in a dense primordial cluster, using the AMUSE framework. We consider both constant mass loss fractions as well as analytic models based on the stellar structure of the colliding stars, and study 6 different accretion models. In constant mass loss scenarios we vary the mass lost during a collision in our simulations, and perform 5 simulations for each accretion scenario, and also when using analytic models. Our calculations indicate that mass loss can significantly affect the final mass of the possible SMBH seed. Considering a constant mass loss of 5% for every collision, the most massive object can lose between 60-80% of the total mass that is obtained if mass loss were not considered. Using instead analytical prescriptions for mass loss, the mass of the final object is reduced by 15-40%, depending on the accretion model for the cluster we study. Altogether, we obtain masses of the order of $10^4 M_\odot$, which are still massive enough to be SMBH seeds, implying that the runaway collision model can be successful even when considering mass loss.

Keywords – Population III, black holes, mass loss

Contents

Agradecimientos i
Resumen ii
Abstract iii

1 Supermassive black holes at high redshift and the local Universe 1

2 Formation mechanisms of supermassive black holes 6
2.1 Direct Collapse scenario 6
2.2 Black holes from the First Stars 11
2.3 Runaway collisions in stellar clusters 13

3 The importance of mass loss in collision driven scenarios 18
3.1 Approximations to estimate mass loss 21

4 Numerical Methods 26
4.1 The AMUSE code 27
4.2 The Hermite integration scheme 28
4.3 The Bridge scheme 31
4.4 Numerical Setup 31
4.5 Code adaptation 35

5 Main Results 38
5.1 Simulations considering constant mass loss 38
5.1.1 Restricted scenario where mass is only allowed to increase 38
5.1.2 Unrestricted scenario where mass is also allowed to decrease 46
5.2 Simulations considering the analytical prescriptions 48

6 Summary and Conclusions 53
6.1 Discussion 54

Bibliography 56

List of Tables

3.1 Results of simulations on massive stellar mergers by Gaburov et al. (2008). The model name of the simulations is given in the first column. The masses of the primary and the secondary stars are shown in the second and the third column respectively. The evolutionary state of the parent stars is given in the fourth column: TAMS, HAMS, and ZAMS stand for turn-off age, half-age and zero-age main sequence respectively. The fifth column shows the number of SPH particles in the simulations, and the sixth column the mass loss percentage in each simulation. All the data was taken from Gaburov et al. (2008). 19

4.1 Different accretion models studied. 34

5.1 Average final masses of the most massive object, obtained in simulations for constant mass loss, where $100f$ is the mass percentage retained per collision. For each model the table shows the average final mass after a simulation, the percentage this mass represents in comparison to the total mass obtained without mass loss, and the σ error for the mass. 39

5.2 Overview of the results of the simulations using the mass loss prescriptions by Glebbeek and Pols (2008), and Lombardi et al. (2002) combined with Schleicher et al. (2013) mass-radius relationship for protostars. We including the average final mass, projected f value which corresponds to that final mass in a constant mass loss scenario, percentage of the total mass compared to a scenario without mass loss, and the standard deviation σ for each set of simulations. 51

List of Figures

1.2 Relation between the mass of the central SMBH M_{BH} and the bulge mass $M_{\rm bulge}$ of the host galaxy, for the 35 early-type galaxies with dynamical measurements of the bulge stellar mass in the sample of McConnell and Ma (2013), divided in brightest cluster galaxies (BCG; green) and non-BCG (red). The SMBH masses are measured using the dynamics of stars (stars) or gas (circles). The error bars indicate 68 percent confidence intervals. The black, dotted line represents the best-fitting power-law relation. Adopted from McConnell and Ma (2013). 3

1.3 M $-$ σ relation for the sample of galaxies listed in McConnell and Ma (2013). Brightest cluster galaxies (BCGs) that are also the central galaxies of their clusters are plotted in green, other elliptical and S0 galaxies are plotted in red, and late-type spiral galaxies are plotted in blue. The black hole masses are measured using the dynamics of masers (triangles), stars (stars), or gas (circles). Error bars indicate 68% confidence intervals. Adopted from McConnell and Ma (2013). 4

2.1 Flow chart illustrating the different pathways that terminate with the formation of a seed BH. The path in the left represents the collapse of the first generation of stars which emerged from gas with the abundances expected after recombination ($z \sim 0$). On the right, the other possible path requires the presence of few metals ($z < z_{\rm crit}$) in a gas cloud that will form a disc as it cools, and then a star cluster may be formed, which will experience a runaway collision process producing a massive star or black hole. Alternatively, if the star formation is suppressed, a strong inflow of gas is expected at the center of the cloud originating a super massive star or an IMBH. Adopted from Volonteri (2010). 7

2.2 Estimates of the critical value of the UV flux required for the direct collapse scenario in a $10^7 M_\odot$ gas cloud. One zone and 3D models of a representative halo are presented, including variations from three different simulated haloes (green triangles). Also there is a red cross showing the results of including an X-Ray background, which makes little difference. 3D simulations and one-zone calculations differ by about two orders of magnitude due to the inability of one-zone models to simulate shocks, collapse dynamics and hydrodynamical effects. Adopted from Latif et al. (2015). 10
2.3 Resultant mass distributions of Pop III.1 (left) and III.2D (right) stars for the different redshifts. The different colours represent different redshift ranges. The black solid lines show the total distributions over all redshifts for each population whereas the dotted lines show the sum of them. Adopted from Hirano et al. (2015). 12
2.4 (Left) Probability of forming a VMS (top) and maximum mass of a VMS (bottom) as a function of cluster mass. (Right) Probability of forming a VMS (top) and maximum mass of a VMS (bottom) as a function of initial central density. Both the probability of forming a VMS and that mass to which a VMS grows to are extremely sensitive to the cluster mass and initial central density. Data points represent results from simulations while solid lines represent linear fits to the data. All data was taken from Katz et al. (2015). . . . 15
2.5 Top panel: mass evolution of the runaway star ($M_{\rm max}(t)/M_{\rm ini}$) in a cluster with $N = 5000$ stars. Each of these stars has an initial mass of $M_{\rm star} = 2M_\odot$ and an initial radius of $R_{\rm star} = 200R_\odot$. Middle panel: the number of collisions ($N_{\rm col}$) as function of the crossing time of the cluster is shown. The red line is the best Gaussian fit. Bottom panel: the mass growth rate $\mathrm{d}M/\mathrm{d}t$ in $M_{\rm ini}\ T_{\rm cr}^{-1}$ is shown. Adopted from Reinoso et al. (2018). 16
2.6 Time evolution of the maximum mass in the system, for six different accretion models and standard set of parameters. Except for model 5, all models efficiently convert at least half of the initial gas mass into one single massive object. Adopted from Boekholt et al. (2018). 17

3.1 Comparing the growth of a VMS due to collisional runaway with and without stellar evolution at solar metallicity. Without stellar evolution (black line) , the direct N-body experiment predicts that this star will grow from an initial mass of $92.4M_\odot$ to a final mass of $1118.9M_\odot$. When stellar evolution, stellar winds and mass loss due to the collision are included (red line), the VMS cannot maintain a large mass and ends up having a final remnant black hole mass of $13.9M_\odot$. The data was taken from Glebbeek et al. (2009). 20

3.2 Dependence of f on the mass ratio q, for the Equations 3.15 and 3.16, labeled with the respective timescale that each equation represents, and also compared with the mass loss values by Gaburov et al. (2008) in Table 3.1. For all possible q values, the value of f never gets below 0.9. 24

4.1 Time evolution of the mass of the central object, for six different accretion models. All models, except for number 5, efficiently convert gas mass into one massive object. Here no mass loss is assumed during the collisions. 32
4.2 Parametrizations of the mass–radius evolution of accreting Pop. III protostars based on Hosokawa et al. (2012). The different colors represent different parametrizations for different accretion rates. Adopted from Boekholt et al. (2018). 33

5.1 Fraction of stars over time corresponding to four categories: escapers (red); stars that have collided with and are part of the most massive star in the system (green, 'Massive object'); stars that are part of other collision products (orange, 'Collision prod.'); and single stars (blue), for different models, and different values for the fraction of mass conserved after a collision f. The general trend for the models is that the fraction of stars being part of the most massive object decreases when f decreases. Adopted from Alister Seguel et al. (2020). 40
5.2 Correlation of the time evolution of the collision and escape rate (bottom panel) with: total star and gas mass (top panel), fraction of stars belonging to the same four categories as in Fig. 5.1 (second panel), and maximum stellar radius and average stellar radius of the remaining stars (third panel), for three different and representative values of the retained mass fraction f. Adopted from Alister Seguel et al. (2020). 42
5.3 Same as Fig. 5.2 for model 3. Adopted from Alister Seguel et al. (2020). 43
5.4 Same as Fig. 5.2 for model 5. Adopted from Alister Seguel et al. (2020). 44
5.5 Final mass of the most massive object at the end of each simulation, as a function of the retained mass fraction f, for each model described. The bar at each point simulated represents the σ error considering 5 simulations for each f per model. Adopted from Alister Seguel et al. (2020). 45

5.6 Time evolution of the mass of the central object, for six different accretion models considering a 10% mass loss per collision. On the left we show a restricted model (a) which only allows mass to increase, and on the right an unrestricted model which allows mass to decrease after a collision. All models, except for number 5, efficiently convert gas mass into one massive object. Adopted from Alister Seguel et al. (2020). 47
5.7 Comparison of models where the mass of the most massive object can only increase (black line) after a collision, and models that allow a decreasing mass (red). Each point in each plot has a bar representing the σ error considering 5 simulations for each retained mass fraction f per model. Adopted from Alister Seguel et al. (2020). 49
5.8 Dependence of f on the mass ratio q, for the Equation 3.2 from Glebbeek and Pols (2008). For all possible q values, the value of f never gets below 0.92 50
5.9 Results of simulations using the mass loss prescriptions by Glebbeek and Pols (2008), and Lombardi et al. (2002) combined with Schleicher et al. (2013) mass-radius relationship for protostars. These results are compared with the restricted constant mass loss scenario. The dashed line in each plot represents the simpler prescription given by Equation 3.2, meanwhile the dash-dotted line represents the results of the more complex parametrization given by Equation 3.1 .Each line represents the mean of final mass for 5 simulations. Adopted from Alister Seguel et al. (2020). 52

Chapter 1

Supermassive black holes at high redshift and the local Universe

Modern astronomy is still trying to explain how the Universe evolved during its early stages. One of the subjects of particular interest is to understand the formation of the first black holes, and their evolution to the present day. On the observational side, studying these early times presents a difficult task due to our technological limitations, but the new generations of telescopes will prove to be useful tools, and will help to confirm or disprove the models that theoreticians have been developing on the matter since a long time.

The models of early black hole formation ought to predict the Supermassive Black Holes (SMBH) we see today. Due to the fact that black holes from the early universe have had more than 12 Gyr time to grow, it is no surprise that SMBHs exist in the local Universe. For example a SMBH with a mass of $4 \times 10^{10} M_{\odot}$ was found at the center of Holmberg 15A, a galaxy 216 Mpc away in the Abell 15 galaxy cluster (Mehrgan et al., 2019). Also, the Milky Way itself has a SMBH at its center, with a mass of $4 \times 10^{6} M_{\odot}$ at a distance of $R_0 = 7.9$ kpc (Boehle et al., 2016). The most distant quasar known to date is ULAS J1342+0928, which hosts the oldest known supermassive black hole, with a mass of $8 \times 10^{8} M_{\odot}$ at a redshift of $z = 7.54$ (Bañados et al., 2018). This quasar is situated at a cosmic age of just 690 Myr after the Big Bang, at times when conditions in the Universe were changing rapidly. The second most distant quasar known is ULAS J1120+0641 at a redshift of 7.085, which is 0.77 billion years after the Big Bang (Mortlock

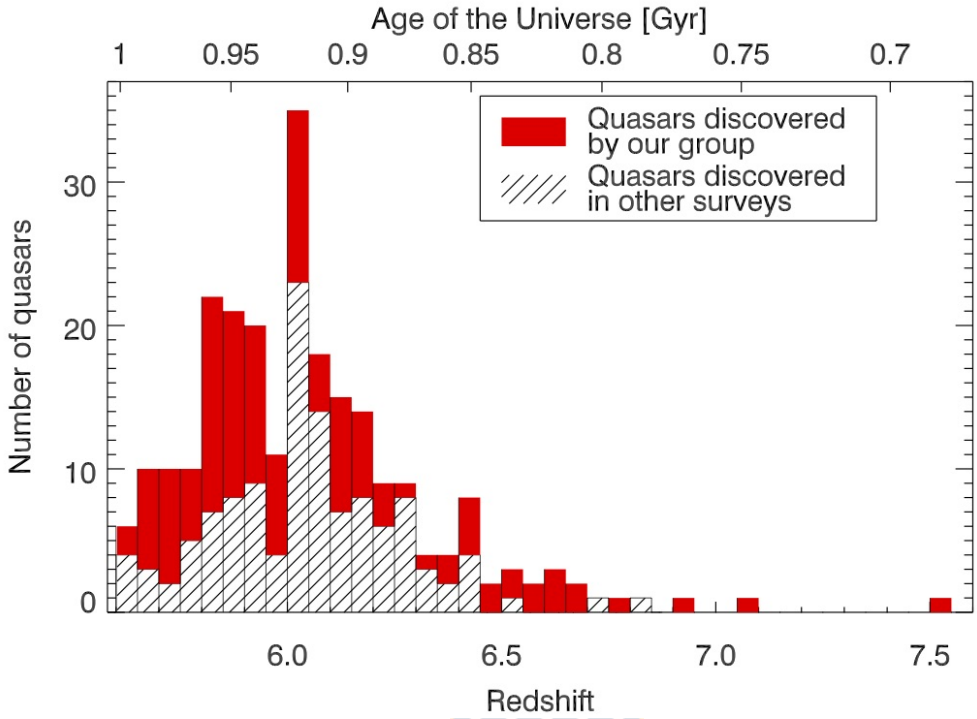

Figure 1.1: Adopted from B. Venemans Research website[1]. Redshift distribution of all $z > 5.6$ quasars known until December 2017. Discoveries of various groups of $\sim$ 120 quasars are shown in the hashed histogram. In the last few years, the Max Planck Institute for Astrophysics group, led by F. Walter and B. Venemans has discovered an additional 125 quasars in various optical and near-infrared surveys, shown in the red histogram, more than doubling the number of quasars at $z > 5.6$.

et al., 2011), and the number of distant quasars detected is still continuously increasing, Figure 1.1 shows the quasar distribution as a function of the redshift to all quasars known until December 2017. Explaining the existence of these objects provides a significant challenge to our cosmological model; if we consider the Eddington accretion rate, which is the maximum rate at which a black hole can accrete gas in spherical symmetry, initial seed masses of order $10^4 M_\odot$ are required to reach final masses of $10^9 M_\odot$, when realistic spin parameters and accretion disk models are taken into account (Shapiro, 2005). The only solutions are very massive seeds or extended periods of super-Eddington accretion, which can persist in non-spherically symmetric circumstances where the Eddington rate can be breached. Or potentially combinations of both during the formation and early growth of massive black holes (Mayer et al., 2013).

It is now widely accepted that SMBHs which exist at the centre of several nearby

[1] http://www.mpia.de/home/venemans/research.html

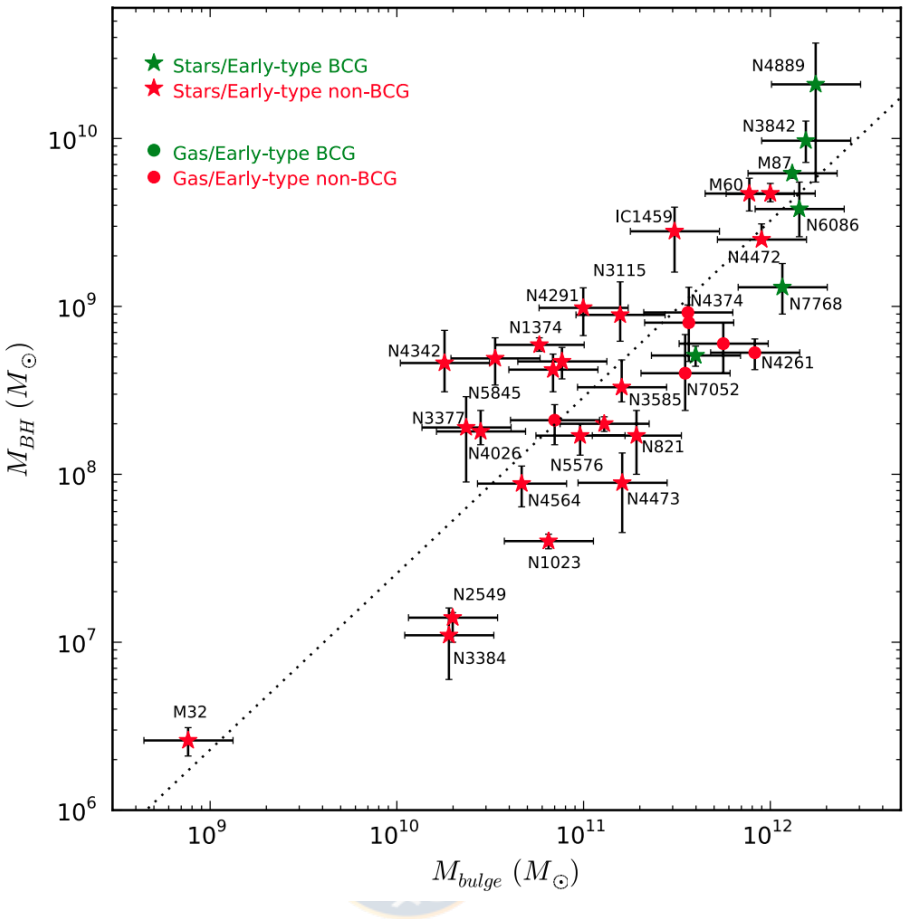

Figure 1.2: Relation between the mass of the central SMBH M_{BH} and the bulge mass $M_{\rm bulge}$ of the host galaxy, for the 35 early-type galaxies with dynamical measurements of the bulge stellar mass in the sample of McConnell and Ma (2013), divided in brightest cluster galaxies (BCG; green) and non-BCG (red). The SMBH masses are measured using the dynamics of stars (stars) or gas (circles). The error bars indicate 68 percent confidence intervals. The black, dotted line represents the best-fitting power-law relation. Adopted from McConnell and Ma (2013).

massive galaxies, and are believed to exist in many high-redshift galaxies, are the engines of AGNs. Accurate mass measurements of the central SMBH masses in the local Universe led to scaling relations between the mass of the central object and other galactic quantities. Two of these quantities, i.e., the most important ones, being the stellar velocity dispersion and the stellar bulge mass. In particular, a tight scaling relation has been found between the SMBH mass M_{BH} and bulge mass $M_{\rm bulge}$, the so-called Magorrian relation (Magorrian et al., 1998),

$$\frac{M_{BH}}{10^9 M_\odot} = 0.49^{+0.06}_{-0.05} \left(\frac{M_{\rm bulge}}{10^{11} M_\odot} \right)^{1.17 \pm 0.08} .$$

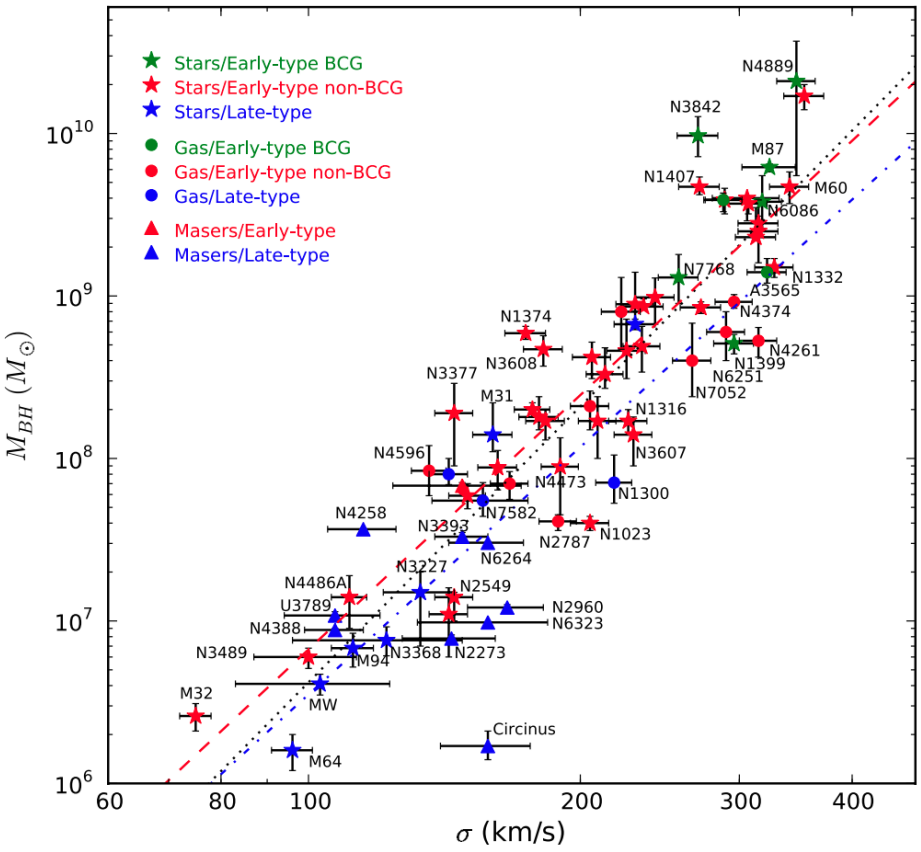

Figure 1.3: M $-$ σ relation for the sample of galaxies listed in McConnell and Ma (2013). Brightest cluster galaxies (BCGs) that are also the central galaxies of their clusters are plotted in green, other elliptical and S0 galaxies are plotted in red, and late-type spiral galaxies are plotted in blue. The black hole masses are measured using the dynamics of masers (triangles), stars (stars), or gas (circles). Error bars indicate 68% confidence intervals. Adopted from McConnell and Ma (2013).

Observational data supporting this relation is shown in Figure 1.2, from McConnell and Ma (2013), who compiled a sample of 72 black holes and their host galaxies, and presented revised scaling relations. Another well restrained scaling relation is the one between the SMBH mass and the effective velocity dispersion σ, the so-called M-σ relation,

$$\frac{M_{BH}}{10^9 M_\odot} = 0.310^{+0.037}_{-0.033} \left(\frac{\sigma}{200 \text{ km s}^{-1}} \right)^{4.38 \pm 0.29} .$$

McConnell and Ma (2013) also presented the M $-$ σ relation for their compilation of 72 dynamical black hole measurements, shown in Figure 1.3.

The above relations are consistent with a scenario in which SMBHs and their host galaxies may co-evolve; SMBHs grow through gas accretion and mergers and feed back part of their accretion energy to the host galaxy. Although, there are alternative explanations for the origin of the scaling relations, which do not require co-evolution. For example, the Magorrian relation could be partly or fully caused by the hierarchical assembly of SMBH and stellar mass through galaxy merging.

Despite the enormous advances in BH physics and astrophysics, we still do not know for certain how these objects have formed in the first place. This is a fundamental question that has been addressed several times through the years.

In our investigation, presented in this thesis, we explore the effect of mass loss during stellar collisions. It is the continuation of our investigation into a SMBH formation scenario, which uses runaway collisions between Population III (Pop. III) stars to form the seeds of the future SMBHs. In our case study Pop. III stars are located in dense stellar clusters. The different formation scenarios of SMBHs are described in Chapter 2, the importance of the mass loss in runaway scenarios, and also our approach to find an analytical prescription are described in Chapter 3, the numerical methods used for our simulations are described in Chapter 4, including our setup and the coding of our mass loss prescription. The main results are presented in Chapter 5. We summarize our work and give the main conclusions in Chapter 6.

Chapter 2

Formation mechanisms of supermassive black holes

The three main pathways for the formation of SMBHs are: i) stellar remnants in the context of massive Pop. III stars, ii) the collapse of a protogalactic gas cloud into a massive black hole or a massive star, that later collapses into a black hole, and iii) seed black holes forming in dense stellar clusters via dynamical processes (Rees, 1984; Woods et al., 2018). A diagram showing the different paths for the formation of massive black holes in the early Universe is presented in Figure 2.1.

2.1 Direct Collapse scenario

One of the most promising explanations for massive seed formation is the direct collapse model, as it can potentially produce the most massive objects. This scenario involves the collapse of a gas cloud into one massive object. The idea for the formation of a massive black hole directly via the gas dynamical processes was conceived in the pioneering work of Martin Rees (Rees, 1984). The expectation is that gas in a low spin halo collapses and forms a rotationally supported compact disk, which later may lead to the formation of a massive black hole (Loeb and Rasio, 1994). In order for the gas to rapidly collapse, the fundamental requirement is that the cloud efficiently transports angular momentum and avoids fragmentation. For the purpose of creating a massive object of $10^4 - 10^6$ $M_\odot$, large inflows (0.1 $M_\odot$/yr) of gas need to be brought into the halo centre within a short time scale of about 1 Myr. Keeping the gas warm will help to obtain such large inflow rates,

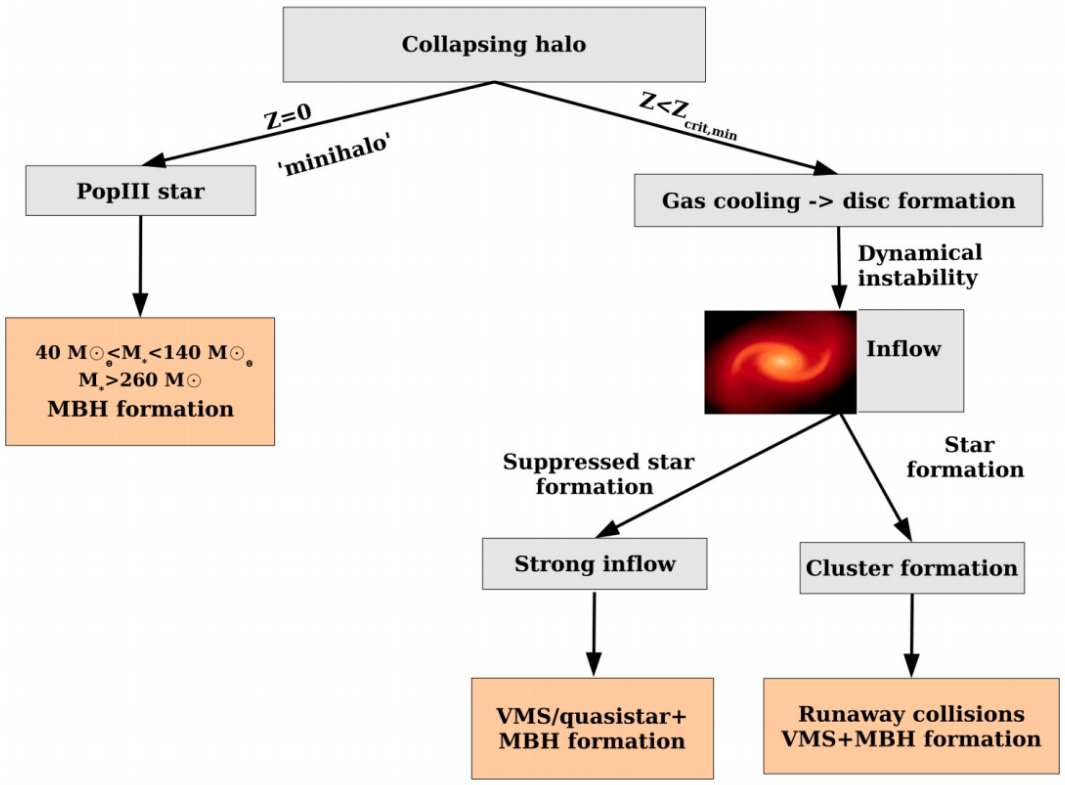

Figure 2.1: Flow chart illustrating the different pathways that terminate with the formation of a seed BH. The path in the left represents the collapse of the first generation of stars which emerged from gas with the abundances expected after recombination ($z \sim 0$). On the right, the other possible path requires the presence of few metals ($z < z_{\rm crit}$) in a gas cloud that will form a disc as it cools, and then a star cluster may be formed, which will experience a runaway collision process producing a massive star or black hole. Alternatively, if the star formation is suppressed, a strong inflow of gas is expected at the center of the cloud originating a super massive star or an IMBH. Adopted from Volonteri (2010).

and depending on the time evolution of mass inflow rates, the central object may form a supermassive star or directly collapse into a massive black hole.

If accretion is regulated by the self-gravity of the gas, the mass inflow rate of collapsing gas $\dot{M}$ is related to its thermodynamical properties in the following way:

$$\dot{M} \sim \frac{c_s^3}{G} \sim 0.1 M_\odot/\mathrm{yr} \left(\frac{T}{8000K}\right)^{3/2}, \tag{2.1}$$

where c_s is the sound speed and T is the gas temperature. This expression can be obtained by dividing the Jeans mass by the free-fall time of the gas. The higher the temperature the larger the mass inflow rate. Therefore, the thermodynamical requirement for getting large inflows is that gas should not cool down to lower temperatures, otherwise it will fragment and form ordinary stars. The cooling ability of the gas is determined by its chemical composition. In primordial gas, molecular hydrogen cooling can bring the gas temperature down to $\sim$ 200 K and induces star formation. In the absence of molecular hydrogen, primordial gas remains in the atomic phase, cools mainly via atomic line radiation and the gas temperature remains around 8000 K.

The potential birthplaces for massive black holes are primordial halos deprived of H_2 cooling. The prerequisites for the formation of massive black holes in atomic cooling halos are that they should be metal-free and the formation of molecular hydrogen remains suppressed. Numerical simulations have shown that this can be achieved when a strong radiation background photodissociates the molecular hydrogen, therefore preventing strong fragmentation of the gas cloud (Bromm and Loeb, 2003; Wise et al., 2008; Latif et al., 2013).

Trace amount of H_2 can be formed via gas phase reactions where a residual fraction of electrons from the recombination epoch acts as a catalyst. The main pathway for the formation of H_2 is the following:

$$\mathrm{H} + e^- \rightarrow \mathrm{H}^- + \gamma \tag{2.2}$$

$$\mathrm{H} + \mathrm{H}^- \rightarrow \mathrm{H}_2 + e^-. \tag{2.3}$$

The H_2 can be dissociated either directly or indirectly by UV radiation. The low energy photons with 0.75 eV can photo-detach H^- which is the main channel for the formation of H_2. The photons with energy between 11.2 - 13.6 eV photo-

dissociate molecular hydrogen via the so called Solomon process, a two-step photo-dissociation process. These processes are described by the following reactions:

$$H^- + h\nu \rightarrow H + e^- \tag{2.4}$$

$$H_2 + h\nu \rightarrow H + H. \tag{2.5}$$

The competition between the formation and dissociation timescales defines the critical value of the UV flux (parametrized by J_{21}), above which the formation of H_2 remains quenched. This value is described through the strength of the radiation background at 13.6 eV. This flux is normalized such that $J_{21} = 1$ corresponds to a radiative background of 10^{-21}erg/s/cm^3/Hz/sr. The first numerical investigations suggested a critical value of $J_{21} \sim 100$ to prevent the formation of molecular hydrogen (Shang et al., 2010), while updated chemical networks and more realistic models for the radiation background (see e.g. Sugimura et al., 2014; Agarwal and Khochfar, 2014) have led to much larger critical values of the order of 10^4 to 10^5 when applied in cosmological simulations (Latif et al., 2014, 2015). In their study, Latif et al. (2015) computed the critical value the J_{21} flux for spectra of Pop II stars through three-dimensional cosmological simulations and one zone models, varying the radiation spectra. Their findings show that the value of weakly depends on the adopted radiation spectra in the range between $T_{rad} = 2 \times 10^4$ and 10^5 K. For three simulated haloes of a few times $10^7 M_\odot$, J_{21} varies from 2×10^4 to 5×10^4. The impact of X-ray ionization is almost negligible. The differences between the one-zone and 3D simulations come from the inability of one-zone models to simulate shocks and hydrodynamical effects. This is resumed in Figure 2.2. In the end, the need for large values of J_{21} provides a problem for the direct collapse scenario (Dijkstra et al., 2014).

In addition to molecular hydrogen line cooling, fragmentation can also be induced via metals or dust grains (Omukai et al., 2008). In the case of metal line cooling, a metallicity of 10^{-3} $Z_\odot$ can already increase the cooling and trigger fragmentation within cosmological simulations (Bovino et al., 2014), while even lower metallicities of 10^{-5} $Z_\odot$ are sufficient when dust cooling is considered (Schneider et al., 2006; Dopcke et al., 2013; Bovino et al., 2016). The need to both have very strong radiation backgrounds, while keeping the gas metal free, leads to a strong need of fine-tuning, which at best can be satisfied under very rare conditions (eg, Agarwal et al., 2017). Recently, Suazo et al. (2019) studied the formation of SMBH seeds in

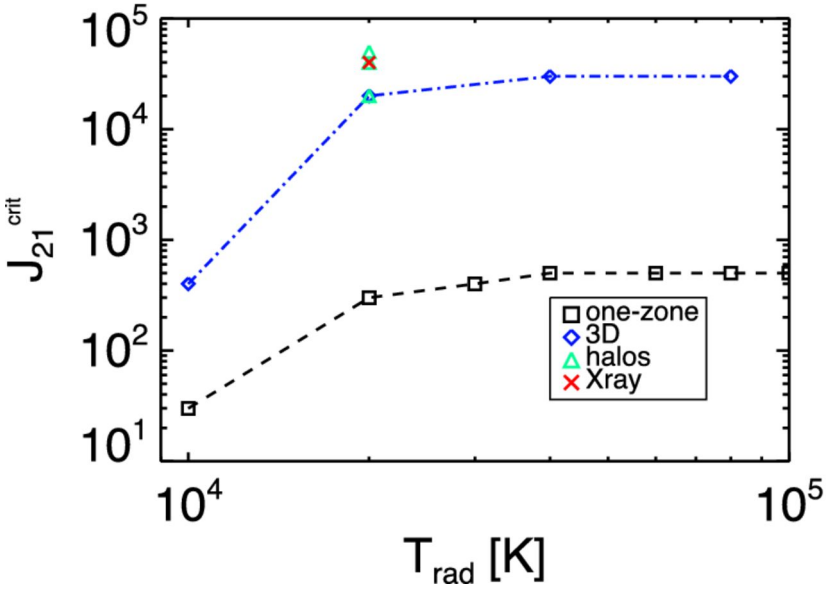

Figure 2.2: Estimates of the critical value of the UV flux required for the direct collapse scenario in a $10^7 M_\odot$ gas cloud. One zone and 3D models of a representative halo are presented, including variations from three different simulated haloes (green triangles). Also there is a red cross showing the results of including an X-Ray background, which makes little difference. 3D simulations and one-zone calculations differ by about two orders of magnitude due to the inability of one-zone models to simulate shocks, collapse dynamics and hydrodynamical effects. Adopted from Latif et al. (2015).

this context, forming a single massive object of $\sim 10^5 M_\odot$ when the UV background of J_{21} is set to 10000, while when considering a UV background of $J_{21} = 10$, there is fragmentation and the formation of various less massive seeds. These fragments have masses of $10^3 - 10^4 M_\odot$, and even though less massive, they were still prone to merge into a more massive object.

2.2 Black holes from the First Stars

The first generation of stars, the Population III stars, were made from metal-free primordial gas in dark matter haloes. This gas was mainly composed of hydrogen and helium. The main cooling mechanism here is molecular hydrogen cooling. This cooling is less efficient than in the present Universe where metals and dust are present. The temperature of the gas in the star forming regions of the early Universe was about 300 K, whereas the molecular clouds of the present day Universe have a temperature of about 10 K. Due to these high temperatures, the thermal pressure, and therefore, the Jeans mass of the gas clouds, were enhanced by a factor of about 100. Today the typical stellar mass is $1 M_\odot$, so we could expect that in the early universe the typical stellar mass was $100 M_\odot$. It has long been thought that the first stars lived short lives, with only one massive star forming in each dark matter halo. Those dark matter minihalos possessed masses around $10^5 - 10^6 M_\odot$ at redshift $z \sim 20 - 25$.

As mentioned in the previous chapter, there are massive quasars with masses around $10^9 M_\odot$ at redshifts of $z = 6$ or above, which provide indirect support for the existence of supermassive stars in the early Universe. Stellar evolution calculations with very high accretion rates suggest that stars could be stable up to several $10^5 M_\odot$, before the general relativistic instability (Chandrasekhar, 1964) leads to the collapse into a black hole of the same mass (Hosokawa and Omukai, 2009; Woods et al., 2018).

Another important process occurring in protostars is the mass accretion, which is expected to be very high in the early Universe , and plays a huge role in determining the mass of a protostar. According to Hosokawa and Omukai (2009), the formation of massive stars by accretion requires an accretion rate of $\dot{M} > 10^{-4} M_\odot$ yr^{-1} to overcome the radiation pressure from the forming star, in order to keep accreting mass once the star has ignited hydrogen in the core.

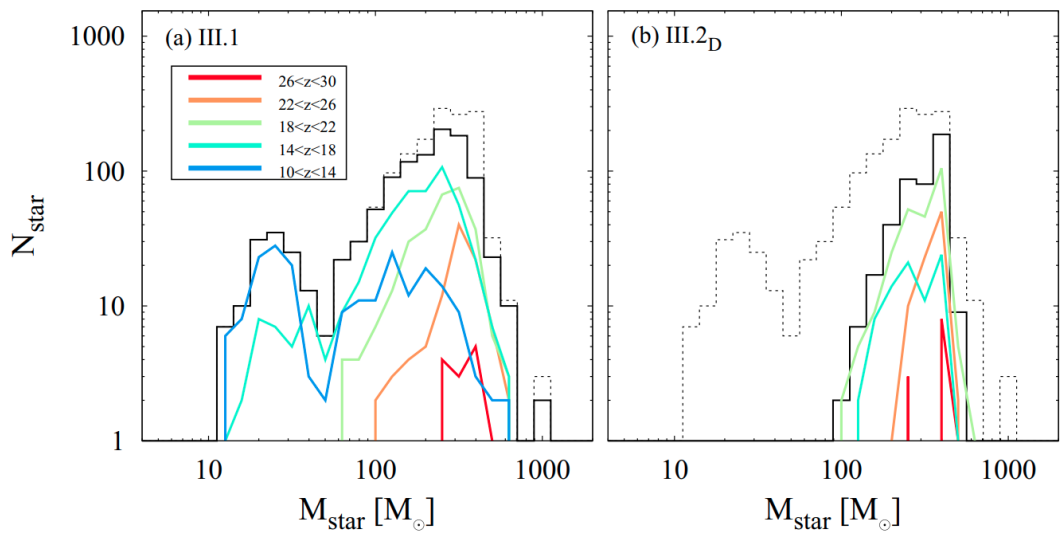

Figure 2.3: Resultant mass distributions of Pop III.1 (left) and III.2D (right) stars for the different redshifts. The different colours represent different redshift ranges. The black solid lines show the total distributions over all redshifts for each population whereas the dotted lines show the sum of them. Adopted from Hirano et al. (2015).

Hirano et al. (2015) performed a large set of cosmological simulations of early structure formation and followed the formation and evolution of 1540 star-forming gas clouds to derive the mass distribution of primordial stars. The star formation in their cosmological simulations is characterized by two distinct populations, the so-called Population III.1 stars and primordial stars formed under the influence of far-ultraviolet radiation (Population III.2D stars). These results are shown in Figure 2.3.

Today many researchers in this field agree that genuine Pop. III stars formed in binary stellar systems or systems of a higher order, and that they had a wide range of masses. The mass scale depends on physical processes such as radiative feedback, the level of turbulence in the halo gas and accretion disk, properties of the dark matter, or the larger scale environment of the star forming halo. Since low-mass Pop. III stars must have survived until the present days, they should be detectable in stellar archeological surveys in the Milky Way and neighboring satellite galaxies, which would help to put constraints in the low-mass end of the Pop. III IMF.

Theoretical limits, from including general relativistic instabilities in the stellar structure equations, predict an upper mass limit of several $10^5 M_\odot$ for primordial

stars. Indeed, these stars could be the seeds for the observed very massive quasars, when able to maintain high accretion rates close to the Eddington limit down to $z > 6$.

2.3 Runaway collisions in stellar clusters

The alternative pathway of black hole formation through stellar clusters has been investigated to a lesser degree in the context of early Universe black hole formation. In these star clusters, a very massive star (VMS) may form through repeated stellar collisions and mergers which may collapse directly to an intermediate mass black hole (IMBH) if the star becomes massive enough.

The galaxies formed in the early Universe were much more dense than those we observe in the local Universe, therefore it is likely that the first star clusters which formed were also significantly denser compared to those observed nearby. In our local neighbourhood, the most extreme systems can reach stellar densities of $10^5 M_\odot/\mathrm{pc}^3$ (Espinoza et al., 2009). As these densities are very high, stellar collisions and mergers are expected to be recurring.

The core collapse and relaxation timescales, besides the main sequence lifetime of massive stars , are very short compared to the age of the Universe when these primordial systems formed. Consequently, at these high stellar densities, it is expected that the mass of the most massive star to form in the cluster is not set by the fragmentation properties of the gas, but rather by the number of mergers and collisions between high mass stars, building a VMS in a dynamical process.

The dynamical process for forming an IMBH seed from collisional runaway proceeds as follows:

- A dense primordial star cluster forms in a metal enriched gas cloud in the early Universe with total mass M_c, radius R_c, total number of stars N, and stellar density n. This star cluster will have a given stellar IMF, virial ratio Q, which determines whether the initial velocities of the star cluster are dynamically cold, hot, or virialized, a binary fraction b, a fractal degree D, as well as a degree of mass segregation S. In the absence of gas, direct N-body experiments show that the star cluster will become spherical rather quickly (Katz et al., 2015) and the shape of the cluster in the initial conditions

weakly affects the final outcome.

- Once the star cluster has formed, the massive stars sink to the center of the cluster due to dynamical friction. This increases the collision probability of stars in the cluster, as the cross sections of these stars are much larger than their lower mass counterparts. Once a collision or merger has occurred, the cross section of the newly formed star increases thus enhancing the probability for a future collision or merger. This process is clearly unstable as the star with the largest cross section is most likely to dominate all subsequent collisions or mergers in the cluster.
- After the collision timescale in the cluster becomes larger than the main sequence lifetime of the VMS, the star cluster will continue to evolve normally without many more stellar collisions or mergers. The VMS then evolves off the main sequence and depending on its mass and metallicity, it may directly collapse to an IMBH with minimal mass loss (Heger et al., 2003).

This is a simple SMBH seed forming mechanism. Furthermore, the conditions needed to initiate the process of collisional runaway have been observed in the local Universe (stellar densities high enough that lead to stellar interactions). For this reason, collisional runaway remains being explored, as this scenario could be the dominant seeding mechanism for high redshift SMBHs.

Analytical models by Devecchi and Volonteri (2009) consider the case where metal enriched birth clouds form at the centers of atomic cooling haloes at high redshift. In this model, they assumed that Pop. III star formation occurs in the low mass mini-haloes which merge to form the more massive object, therefore setting the global metallicity of the halo above the critical value needed for efficient fragmentation. They assume that a gaseous disk forms and that the Toomre parameter, a criterion for the stability of differentially rotating disks (Toomre, 1964), is sufficiently high so that the disk does not fragment efficiently. This allows a massive star cluster to form in the center of the disk which may undergo collisional runaway. They predict black hole masses of $100 - 1000 M_{\odot}$ forming in these stellar clusters. Katz et al. (2015) attempted a different approach where they aimed to form the birth clouds of high redshift Population II star clusters from first principles, using star cluster initial conditions constrained from high resolution cosmological simulations. They presented complete studies which tested

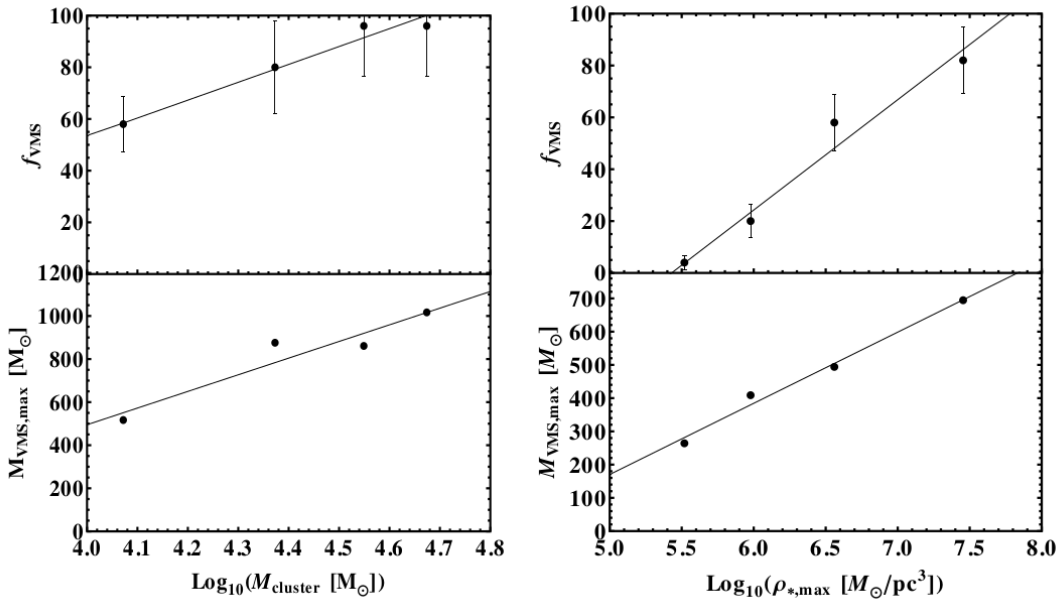

Figure 2.4: (Left) Probability of forming a VMS (top) and maximum mass of a VMS (bottom) as a function of cluster mass. (Right) Probability of forming a VMS (top) and maximum mass of a VMS (bottom) as a function of initial central density. Both the probability of forming a VMS and that mass to which a VMS grows to are extremely sensitive to the cluster mass and initial central density. Data points represent results from simulations while solid lines represent linear fits to the data. All data was taken from Katz et al. (2015).

the multitude of star cluster parameters which may affect the growth of a VMS.

In Figure 2.4, we use the results from Katz et al. (2015) and show how the probability of forming a VMS in a given cluster as well as the mass of a VMS changes as a function of initial central density and mass. As the mass and initial central density are increased, both the probability of forming a very massive star and the maximum mass a very massive star can increase considerably. These models showed the subsequent formation of a $\sim 1000 M_\odot$ black hole.

The properties of high redshift star clusters are still highly unconstrained. This is being addressed via a combination of cosmological and N-body simulations to sample multiple haloes and constrain the properties of primordial star clusters in the work of Sakurai et al. (2017), which also showed the formation of black holes in the first stellar clusters with $400 - 1900\ M_\odot$. Reinoso et al. (2018) studied collisions in massive Pop. III clusters, showing there could be resulting black hole masses of up to $600 M_\odot$. The resulting evolution of one of their simulations is

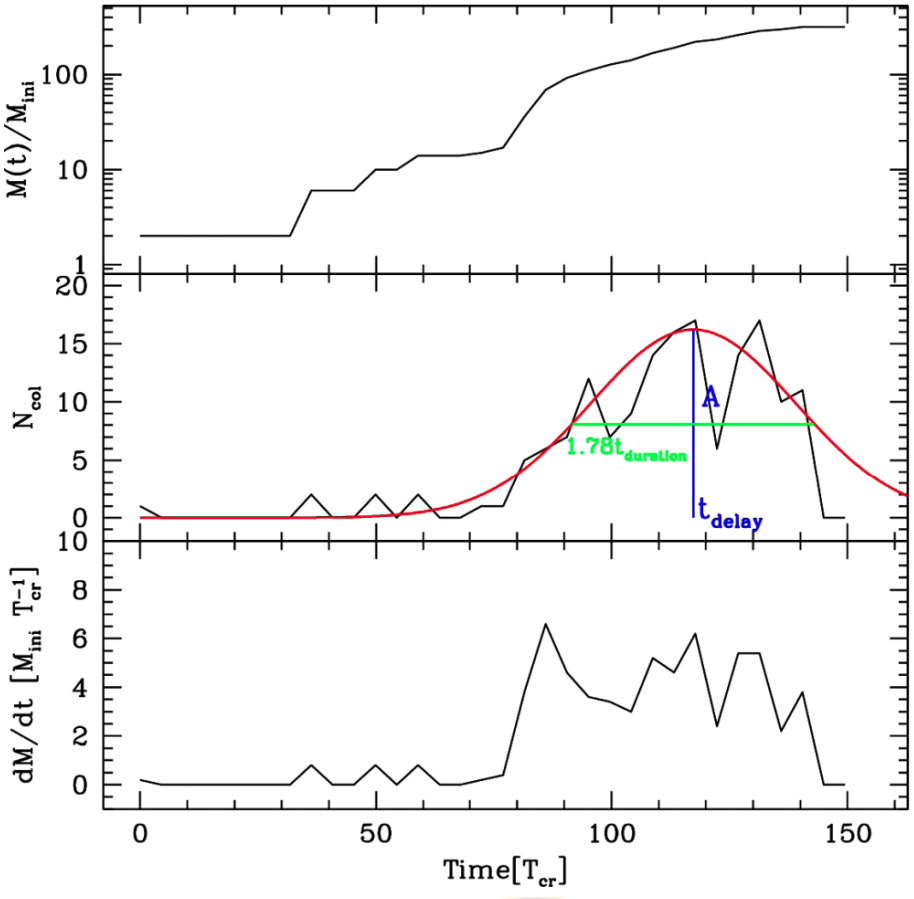

Figure 2.5: Top panel: mass evolution of the runaway star ($M_{\rm max}(t)/M_{\rm ini}$) in a cluster with $N = 5000$ stars. Each of these stars has an initial mass of $M_{\rm star} = 2M_{\odot}$ and an initial radius of $R_{\rm star} = 200R_{\odot}$. Middle panel: the number of collisions ($N_{\rm col}$) as function of the crossing time of the cluster is shown. The red line is the best Gaussian fit. Bottom panel: the mass growth rate $\mathrm{d}M/\mathrm{d}t$ in $M_{\rm ini}\ T_{\rm cr}^{-1}$ is shown. Adopted from Reinoso et al. (2018).

shown in Figure 2.5, to illustrate how runaway-collisions occur in dense clusters.

Boekholt et al. (2018) were the first to explore the formation of massive black hole seeds from a dense stellar cluster, where gas-phase effects like accretion as well as the resulting enhanced protostellar radii were taken into account, considering the interaction between stellar-dynamical and gas-dynamical processes. The initially low mass Pop. III protostars gain mass by accreting from the gas reservoir. Since the accretion rate may vary with cluster environment and cluster evolution, they defined 6 different accretion models, in which accretion depends on the gas availability and position of the protostar. The models are further described in section 4.4 and summarized in table 4.1. The black hole masses evolution

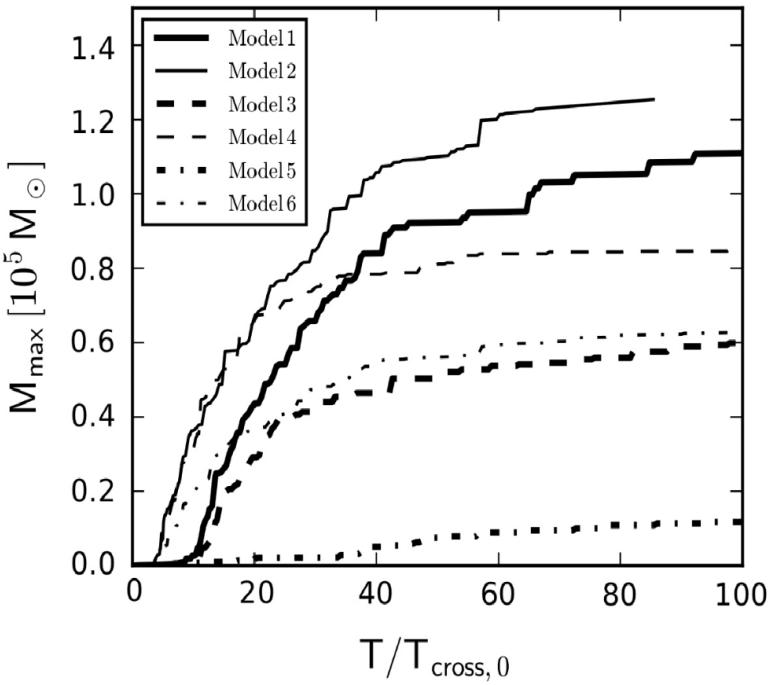

Figure 2.6: Time evolution of the maximum mass in the system, for six different accretion models and standard set of parameters. Except for model 5, all models efficiently convert at least half of the initial gas mass into one single massive object. Adopted from Boekholt et al. (2018).

for a standard set of parameters is shown in Figure 2.6. They concluded that accretion-induced collisions in dense Pop. III protostellar systems, in the presence of a sufficiently large gas reservoir, are a viable mechanism for explaining the formation of the first massive black hole seeds. Stellar collisions in primordial star clusters can give rise to the formation of massive objects of $10^4 - 10^5 M_\odot$ for all the models considered. These topics certainly deserves further exploration and provide a promising channel for the formation of supermassive black hole seeds.

The latter investigation warranted follow up studies, to improve on the realism of the implementation and to include additional physics previously not considered. One important aspect not taken into account was the mass that might get lost whenever two protostars collide, which is the main focus of our study here.

Chapter 3

The importance of mass loss in collision driven scenarios

Mass loss in star collisions potentially plays a huge role in the formation of massive objects in primordial clusters. Collisions of stars have been explored already to a considerable extent, previous works include Dale and Davies (2006), that shows parabolic encounters between low- and high-mass stars and between two high-mass stars with small periastrons, which resulted in mergers on time-scales of a few tens of stellar free-fall times (a few tens of hours). Such mergers of unevolved low mass stars with evolved high-mass stars result in little mass loss; this means between 2-4% of the total mass.

Gaburov et al. (2008) studied mixing in massive stellar mergers, presenting a computationally inexpensive method in which they approximated the merger process, including shock heating, hydrodynamic mixing and mass loss, which was estimated through energy conservation arguments. They found that mass loss is reduced in collisions involving stars of significantly different mass, as less kinetic energy is redirected into the ejecta. Additionally, mass loss was larger in collisions with evolved stars, due to their weakly bound envelopes . Table 3.1 resumes the mass loss in the simulations of Gaburov et al. (2008) work. It is worth noting that the highest mass loss they obtained was 8.9%. Glebbeek and Pols (2008) modelled central collisions between low mass stars, using a prescription by Lombardi et al. (2002) for collisions between main sequence stars, obtaining mass losses of a few percent.

Table 3.1: Results of simulations on massive stellar mergers by Gaburov et al. (2008). The model name of the simulations is given in the first column. The masses of the primary and the secondary stars are shown in the second and the third column respectively. The evolutionary state of the parent stars is given in the fourth column: TAMS, HAMS, and ZAMS stand for turn-off age, half-age and zero-age main sequence respectively. The fifth column shows the number of SPH particles in the simulations, and the sixth column the mass loss percentage in each simulation. All the data was taken from Gaburov et al. (2008).

Model	M_1	M_2	Evolutionary state	N	Mass loss (%)
T88	80	8	TAMS	880k	1.9
H88	80	8	HAMS	880k	0.8
T48	40	8	TAMS	480k	5
H48	40	8	HAMS	480k	2.1
T28	20	8	TAMS	280k	8.9
H28	20	8	HAMS	280k	4.7
Z28	20	8	ZAMS	280k	4.5
T18	10	8	TAMS	180k	8.7
H18	10	8	HAMS	180k	6.8
Z18	10	8	ZAMS	180k	6.4

Glebbeek et al. (2009) used results from direct N-Body simulations, and calculated how massive a VMS can become if mass loss due to collisions and stellar winds are taken into account. At solar metallicity, they demonstrate that a star which would grow to over $1000M_{\odot}$ due to collisional runaway when only the N-body dynamics are considered, may actually only become a star of $100M_{\odot}$ at the end of its life due to the significant amount of mass loss when stellar evolution is considered. Figure 3.1, shows the growth of the same VMS in a simulations with and without stellar evolutionary processes from Glebbeek et al. (2009). While the N-body only run conserves all mass which takes part in the collision, by the end of its life time, the VMS which has formed in the run with stellar evolution has lost the majority of its mass due to stellar winds. Even with a considerable amount of mergers, collisional runaway is very unlikely to produce a massive black hole when the cluster is at solar metallicity, due to the heavy mass loss from stellar winds. While stellar winds may prevent the formation of IMBHs in high metallicity clusters at low redshift, the gas at high redshift has a composition much closer to primordial.

At lower metallicities (i.e. at Z=0.001 rather than Z=0.02) the mass loss rates are significantly lower, therefore the VMS can retain much of its mass. The simulations show that VMSs with masses over $260M_{\odot}$ can form at this metallicity,

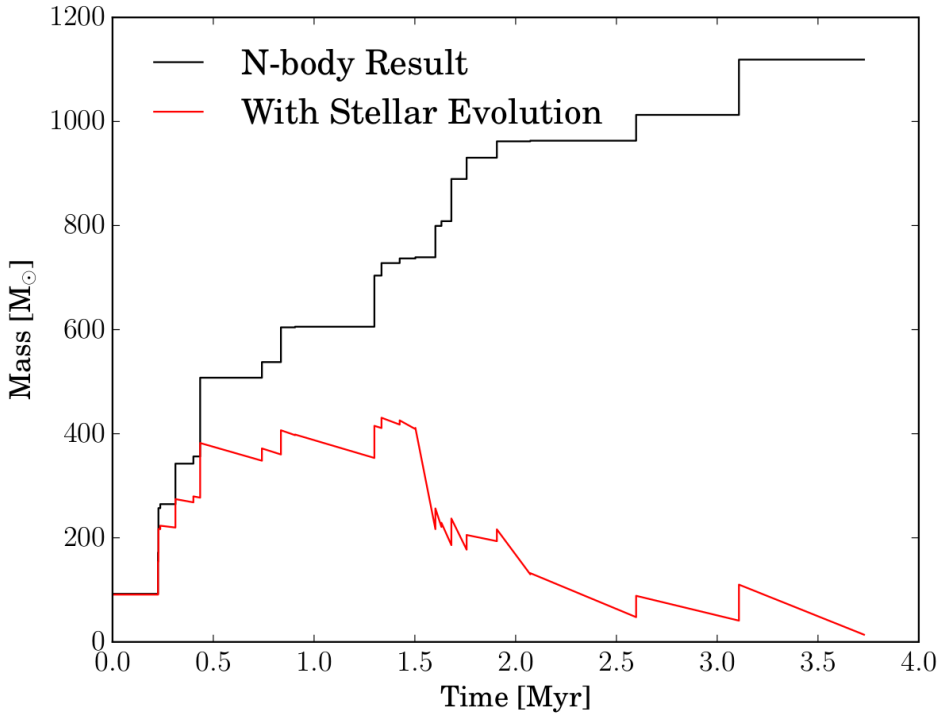

Figure 3.1: Comparing the growth of a VMS due to collisional runaway with and without stellar evolution at solar metallicity. Without stellar evolution (black line) , the direct N-body experiment predicts that this star will grow from an initial mass of $92.4M_{\odot}$ to a final mass of $1118.9M_{\odot}$. When stellar evolution, stellar winds and mass loss due to the collision are included (red line), the VMS cannot maintain a large mass and ends up having a final remnant black hole mass of $13.9M_{\odot}$. The data was taken from Glebbeek et al. (2009).

which suggests that even in the presence of stellar winds, collisional runaway is still a viable process for forming IMBHs at high redshift. Direct N-body simulations generally assume a sticky sphere approach such that if the radii of two stars overlap, then the stars are considered to have merged. However, smooth particle hydro-dynamics simulations which have studied the mergers of stars demonstrate that not all mass which enters the collision is actually retained by the final merger remnant (Dale and Davies, 2006; Trac et al., 2007; Glebbeek et al., 2013). Depending on the orientation of the collision, for example, whether it is a grazing merger or head on collision, different amounts of mass can be lost from the system into the surrounding interstellar medium (Dale and Davies, 2006; Trac et al., 2007). As mentioned before, the amount of mass lost in the collision also depends on the types of stars which were involved in the process (Glebbeek and Pols, 2008). For low metallicity clusters, this effect may be more important than mass loss due to stellar winds (Katz et al., 2015).

In addition to the mass loss during the merger, kinetic energy may be transferred into the envelope of the collision remnant which can cause the cross section to swell by a factor of 100 for some fixed time scale (Dale and Davies, 2006). While this may enhance the probability of future collisions, if too much energy is provided to the envelope after it has been expanded, it can be completely driven off resulting in mass loss which would act against the formation of a VMS (Dale and Davies, 2006).

3.1 Approximations to estimate mass loss

Our aim is to find a realistic prescription for the mass loss fraction. Lombardi et al. (2002) presented simulations of stellar collisions using SPH, providing the following prescription to fit the mass ejected by the collision:

$$\phi = C_1 \frac{q}{(1+q)^2} \frac{R_{1,0.86} + R_{2,0.86}}{R_{1,0.5} + R_{2,0.5}}\,, \tag{3.1}$$

where ϕ is the fraction of mass ejected, $C_1 = 0.1574$, q is the mass ratio M_2/M_1, and $R_{n,0.5}$, $R_{n,0.86}$ are the radii containing 50 and 86 percent of mass of the parent star n (1 or 2). Glebbeek and Pols (2008) found that when the stellar structures

are more equal, the mass-loss could also be modelled using the simpler prescription

$$\phi = C_2 \frac{q}{(1+q)^2} \tag{3.2}$$

with $C_2 = 0.3$.

From Schleicher et al. (2013) we get a mass-radius relationship for accreting primordial protostars:

$$\frac{1000 R_\odot}{R} = \frac{1000}{260 (M/M_\odot)^{1/2}} + \frac{1.04 \mathrm{yr}^{-1} (t - t_{ini}(M))}{M/M_\odot}. \tag{3.3}$$

If the timescale for accretion is much larger than the timescale for protostellar contraction, i.e. $t_{acc} \gg t_{KH}$ the first term on the right-hand side of the equation dominates and we have

$$\frac{1000 R_\odot}{R_n} = \frac{1000}{260 (M_n/M_\odot)^{1/2}}. \tag{3.4}$$

Then we can rearrange terms to get the following

$$R_n = 260 \left(\frac{M_n}{M_\odot} \right)^{1/2} R_\odot. \tag{3.5}$$

Finally we introduce the decimal percentage i of the mass, to calculate the radius which contains that mass

$$R_{n,i} = 260 \left(\frac{i * M_n}{M_\odot} \right)^{1/2} R_\odot. \tag{3.6}$$

Now we can determine the quantities

$$R_{n,0.5} = 260 \left(\frac{0.5 * M_n}{M_\odot} \right)^{1/2} R_\odot, \tag{3.7}$$

$$R_{n,0.86} = 260 \left(\frac{0.86 * M_n}{M_\odot} \right)^{1/2} R_\odot. \tag{3.8}$$

Similarly we analyze the case when t_{KH} dominates, then Equation 3.3 becomes

$$\frac{1000 R_\odot}{R_n} = \frac{1.04 \mathrm{yr}^{-1} (t - t_{ini}(M_n))}{M/M_\odot}. \tag{3.9}$$

Rearranging terms

$$R_n = \frac{M_n}{1.04 \times 10^{-3} M_\odot} \frac{1}{t_{KH}/\mathrm{yr}} R_\odot. \tag{3.10}$$

We can introduce the decimal percentaje i to obtain

$$R_{n,i} = \frac{i * M_n}{1.04 \times 10^{-3} M_\odot} \frac{1}{t_{KH}/\mathrm{yr}} R_\odot. \tag{3.11}$$

And finally calculate the values

$$R_{n,0.5} = \frac{0.5 * M_n}{1.04 \times 10^{-3} M_\odot} \frac{1}{t_{KH}/\mathrm{yr}} R_\odot, \tag{3.12}$$

$$R_{n,0.86} = \frac{0.86 * M_n}{1.04 \times 10^{-3} M_\odot} \frac{1}{t_{KH}/\mathrm{yr}} R_\odot. \tag{3.13}$$

The relevant timescales are given as:

$$t_{acc} = \frac{M}{\dot{M}} \ , \qquad t_{KH} = \frac{GM^2}{RL} \ ,$$

where we assumed L to be the Eddington luminosity, $L_{Edd} = 3.8 \times 10^4 L_\odot (M/M_\odot)$. We can now evaluate in each encounter the final resulting mass as follows

$$M_t = (M_1 + M_2) * (1 - \phi), \tag{3.14}$$

where ϕ is given by equation 3.1. In order to determine ϕ, first we have to evaluate which is the timescale that dominates for each colliding star, then we can use equations 3.7, 3.8, 3.12, and 3.13 to obtain a final mass formula that will depend solely on the mass of the parent stars. Depending on the combination of timescales which dominate the parent star we obtain three cases:

- When t_{acc} dominates for both protostars

$$M_t = (M_1 + M_2) * \left(1 - 0.2059 \times \frac{q}{(1+q)^2}\right). \tag{3.15}$$

- When t_{KH} dominates for both protostars

$$M_t = (M_1 + M_2) * \left(1 - 0.27 \times \frac{q}{(1+q)^2}\right). \tag{3.16}$$

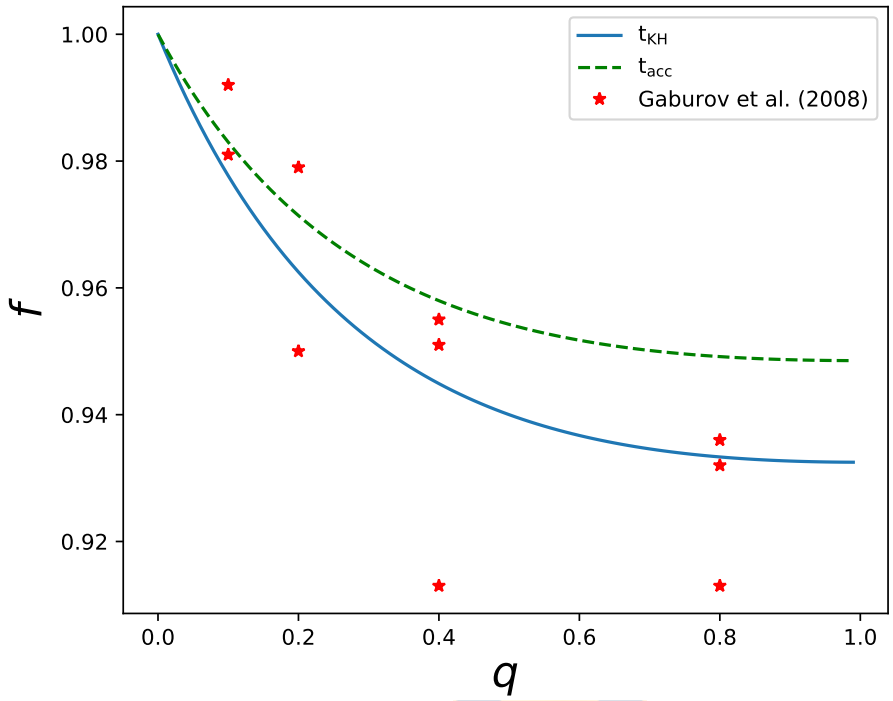

Figure 3.2: Dependence of f on the mass ratio q, for the Equations 3.15 and 3.16, labeled with the respective timescale that each equation represents, and also compared with the mass loss values by Gaburov et al. (2008) in Table 3.1. For all possible q values, the value of f never gets below 0.9.

- When t_{acc} dominates for one protostar, and t_{KH} dominates for the other one

$$M_t = (M_1 + M_2) * \left(1 - \frac{0.157q}{(1+q)^2} \cdot \frac{826(M_2/t_{KH2}) + 241.11M_1^{1/2}}{480.76(M_2/t_{KH2}) + 183.84M_1^{1/2}}\right). \quad (3.17)$$

We note that when the same timescale dominates, the mass loss depends solely on the mass ratio of the components, and when the two stars are dominated by different timescales, the result will depend also on the Kelvin-Helmholtz timescale of the parent star which is dominated by this timescale.

Now we describe the final mass of the collision product as follows:

$$M_t = (M_1 + M_2) * f(M_1, M_2, R_1, R_2), \quad (3.18)$$

where f is a function that regulates the mass loss effect, and is defined by $f = (1 - \phi)$. Due to the nature the obtained equations for the final mass, these equations will have a defined domain for the values that f can reach. We show

this domain for Equations 3.15 and 3.16, also comparing them with the values from Table 3.1, in Figure 3.2. It can be seen that the value of f does not get below 0.9, even for Gaburov et al. (2008) results, which had the larger amounts of mass loss in the investigations we studied (e.g. Dale and Davies (2006), Glebbeek and Pols (2008)). Consequently, we decide that when applying mass loss to our simulations we would not wander too far from these results, considering a range of f from 0.85 to 0.99, enough to cover extreme and conservative cases of mass loss in a hypothetical constant mass loss scenario.

Chapter 4

Numerical Methods

In order to model our astrophysical system, which consists of Pop. III protostars embedded in their natal gas cloud, we consider a variety of physical processes that play a role. These are gravitational N-body dynamics, gravitational coupling between the stars and the gas, stellar growth in mass and size due to gas accretion, and stellar collisions. We adopt the 'sticky-sphere' approximation to treat collisions between protostars: whenever the distance between two protostars is less than the sum of their radii, we replace the two protostars by a single object at the center of mass, with a new mass, and new radius determined by a mass-radius parametrization further described in Section 4.4.

To determine the value of the mass of this new single object, we have to account for the mass loss in the collision. This mass loss fraction should take into account the most important parameters of a collision process. As stated in the previous chapter, the final mass of the collision product will be described as follows:

$$M_t = (M_1 + M_2) * f(M_1, M_2, R_1, R_2) \ , \tag{4.1}$$

where f describes the mass fraction that is kept during the collision, which we can assume here to depend mostly on the stellar mass and the stellar structure. It is conceivable that also the collision velocity may play a relevant role as well as the difference in the dynamics between two-body and three-body mergers, but these need to be explored in more detail via hydrodynamical simulations. It has however been shown in simulations by Gaburov et al. (2010) that the hydrodynamics of 3-body collisions (a binary and a third star) are well-described

with the sticky-sphere approximation plus additional mass loss in at least 75% of all cases. We assume here that the mass being ejected during the merger will be ejected at high velocities, and consequently escape from the gravitational potential. It is therefore not being returned to the gas reservoir.

The literature on stellar mergers tells us that in a collision the mass loss depends on the stellar evolutionary stage (weakly bound envelopes in older stars leads to higher mass loss), mass and collision parameters, and the final product retains between 90% and 100 % of the total mass (Dale and Davies, 2006; Gaburov et al., 2008; Glebbeek and Pols, 2008). In our simulations, we will first assume constant values for the mass loss, and see how a constant mass loss fraction in every collision affects the final mass of the most massive object formed in the cluster. If the final object is massive enough, i.e. reaching at least 1000 $M_{\odot}$, we expect that it will evolve into a massive black hole at the end of its lifetime. So far, simulations of stellar mergers have focused on collisions between main-sequence stars and evolved stellar objects, while collisions between protostars have been explored to a lesser degree in the context of the formation of massive stars (see e.g. Baumgardt and Klessen, 2011). To our knowledge, mass loss in protostellar collisions has not been studied in the context of SMBH seed formation. The latter would be important to better understand the implications of such mergers in scenarios as the ones considered here. In the absence of further information, and in addition to constant mass loss scenarios, we adopt the parametrizations derived by Lombardi et al. (2002) and Glebbeek and Pols (2008) for the mass loss, combining them with approximate protostellar models from Schleicher et al. (2013) (see Sec. 3.1).

4.1 The AMUSE code

We used the Astrophysical Multi-purpose Software Environment (AMUSE, Portegies Zwart and McMillan, 2018; Portegies Zwart et al., 2009, 2013; Pelupessy et al., 2013), which was designed for performing multi-physics simulations as required for this study. AMUSE has been developed at the Leiden Observatory under the supervision of Simon Portegies Zwart. The Leiden Observatory is part of the Leiden University in the Netherlands, while the funding is provided by a NOVA grant. AMUSE is free to download [1] and to use and provides a very simple

[1] http://www.amusecode.org

python interface to existing codes, handling unit conversions so the user can focus more on the coupling strategies for performing multi-physics simulations. AMUSE has the flexibility to introduce a mass-radius parametrization for accreting Pop. III protostars, and to couple it to existing N-body codes. Also, there is currently an AMUSE github that is frequently being debugged by the community[2].

AMUSE contains a variety of codes written in different languages such as `C`, `C++`, and `Fortran`. These codes are usually free source codes such as `ATHENA` or `MESA` and are referred to as community codes. AMUSE provides a `PYTHON` interface where the community codes are loaded and initialized giving them the initial conditions with generic functions such as *code.add_particles(stars)* and then run with functions such as *code.evolve_model(t_end)*. AMUSE provides a simple way to run simulations combining different codes hiding the complexity of the numerical implementations.

We assume that the protostars and the gas are distributed equally, following a Plummer distribution. The protostars will gain mass by accreting from the gas, and their radii are completely determined by the mass and accretion rate, at every time step in our simulation. The star-star gravitational interactions are modelled using the N-body code ph4 (4th order Hermite integrator algorithm in combination with the time-symmetric integration scheme of Hut et al. (1995)), and gravitational dynamics of the gas cloud are included by using an analytical background potential. This potential is coupled to the stars using the BRIDGE method (Fujii et al., 2007), so that the stars experience the gravitational force from each other as well as from the gas.

4.2 The Hermite integration scheme

The Hermite integrator scheme is based on a predictor-corrector scenario, this means, that we will use an extrapolation of the equations of motion to get a predicted position and velocity at some time, then we will use this information to get the new accelerations, then correct the predicted values using interpolation, based on finite differences terms. We can use polynomial adjustment in the gravitational forces evolution over time, because the force acting on each particle changes smoothly.

[2]https://github.com/amusecode/amuse

This algorithm is considered fourth-order, because the predictor considers the contributions of the third order polynomial, then, after obtaining the accelerations, adds a fourth-order corrector term.

Each particle has its own time (t_i), timestep (Δt_i), position ($\mathbf{r}_{i,0}$) and velocity ($\mathbf{v_{i,0}}$) at time t_i, as well as acceleration ($\mathbf{a}_{i,0}$) and time derivative of acceleration ($\dot{\mathbf{a}}_{i,0}$) calculated at time t_i. The mathematical formulation of the main steps of the integration are the following: first we predict the position and velocities of all the particles,

$$\mathbf{r}_{i,pred} = \mathbf{r}_{i,0} + \mathbf{v}_{i,0}\Delta t_i + \frac{1}{2!}\mathbf{a}_{i,0}\Delta t_i^2 + \frac{1}{3!}\dot{\mathbf{a}}_{i,0}\Delta t_i^3 \tag{4.2}$$

$$\mathbf{v}_{i,pred} = \mathbf{v}_{i,0} + \mathbf{a}_{i,0}\Delta t_i + \frac{1}{2!}\dot{\mathbf{a}}_{i,0}\Delta t_i^2. \tag{4.3}$$

Using the predicted positions and velocities from equations 4.2 and 4.3, we evaluate the acceleration and its time derivative for a particle i according to the following:

$$\mathbf{a}_i = \sum_{j\neq i}^{N} Gm_j \frac{\mathbf{r}_{ij}}{(r_{i,j}^2 + \epsilon^2)^{\frac{3}{2}}}, \tag{4.4}$$

$$\dot{\mathbf{a}}_i = \sum_{j\neq i}^{N} Gm_j \left[\frac{\mathbf{v}_{ij}}{(r_{i,j}^2 + \epsilon^2)^{\frac{3}{2}}} + \frac{3(\mathbf{v}_{i,j}\cdot\mathbf{r}_{i,j})\mathbf{r}_i}{(r_{i,j}^2 + \epsilon^2)^{\frac{5}{2}}}\right], \tag{4.5}$$

where

$$\mathbf{r}_{ij} = \mathbf{r}_{j,pred} - \mathbf{r}_{i,pred}, \tag{4.6}$$

$$\mathbf{v}_{ij} = \mathbf{v}_{j,pred} - \mathbf{v}_{i,pred}, \tag{4.7}$$

and ϵ is a softening parameter. The corrector is based on the third order Hermite interpolation constructed using $\mathbf{a}$ and $\dot{\mathbf{a}}$ at times t_i and $t_i + \Delta t_i$. The third order Hermite interpolation polynomials for the acceleration terms are expressed as:

$$\mathbf{a}_i = \mathbf{a}_{i,0} + \Delta t_i \dot{\mathbf{a}}_{i,0} + \frac{\Delta t_i^2}{2!}\mathbf{a}_{i,0}^{(2)} + \frac{\Delta t_i^3}{3!}\mathbf{a}_{i,0}^{(3)} \tag{4.8}$$

$$\dot{\mathbf{a}}_i = \dot{\mathbf{a}}_{i,0} + \Delta t_i \mathbf{a}_{i,0}^{(2)} + \frac{\Delta t_i^2}{2!}\mathbf{a}_{i,0}^{(3)}, \tag{4.9}$$

where $\mathbf{a}_{i,0}$ and $\dot{\mathbf{a}}_{i,0}$ are the acceleration and its derivative calculated at time t_i. We do not know the second and third acceleration derivatives $\mathbf{a}_{i,0}^{(2)}$ and $\mathbf{a}_{i,0}^{(3)}$. However, we can use Equations 4.4 and 4.5 to calculate $\mathbf{a}_i$ and $\dot{\mathbf{a}}_i$, in order to replace them

in equations 4.8 and 4.9. Then it is easy to show that:

$$\mathbf{a}_{i,0}^{(2)} = \frac{-6(\mathbf{a}_{i,0} - \mathbf{a}_i) - \Delta t_{i,0}(4\dot{\mathbf{a}}_{i,0} + 2\dot{\mathbf{a}}_i)}{\Delta t_{i,0}^2} \tag{4.10}$$

$$\mathbf{a}_{i,0}^{(3)} = \frac{-12(\mathbf{a}_{i,0} - \mathbf{a}_i) - 6\Delta t_{i,0}(\dot{\mathbf{a}}_{i,0} + \dot{\mathbf{a}}_i)}{\Delta t_{i,0}^3}. \tag{4.11}$$

where $\mathbf{a}_i$ and $\dot{\mathbf{a}}_i$ are the acceleration and its derivative at the time $t_i + \Delta t_i$. The correction formulae for the position and velocity are expressed now as:

$$\mathbf{r}_i = \mathbf{r}_{i,pred} + \frac{\Delta t_i^4}{4!}\mathbf{a}_{i,0}^{(2)} + \frac{\Delta t_i^5}{5!}\mathbf{a}_{i,0}^{(3)}, \tag{4.12}$$

$$\mathbf{v}_i = \mathbf{v}_{i,pred} + \frac{\Delta t_i^3}{3!}\mathbf{a}_{i,0}^{(2)} + \frac{\Delta t_i^4}{4!}\mathbf{a}_{i,0}^{(3)}. \tag{4.13}$$

Finally, it is necessary to calculate the next time-step for the i particle ($\Delta t_{i,1}$) and time t using the following formulas:

$$t_{i,1} = t_{i,0} + \Delta t_{i,0} \tag{4.14}$$

$$\Delta t_{i,1} = \sqrt{\eta \frac{|\mathbf{a}_i||\mathbf{a}_i^{(2)}| + |\dot{\mathbf{a}}_i|^2}{|\dot{\mathbf{a}}_i||\mathbf{a}_i^{(3)}| + |\mathbf{a}_i^{(2)}|^2}} \tag{4.15}$$

where η is a parameter that controls accuracy, $\mathbf{a}_i$ and $\dot{\mathbf{a}}_i$ are already known, $\mathbf{a}_i^{(3)}$ has the same value as $\mathbf{a}_{i,0}^{(3)}$, due the third-order interpolation; and $\mathbf{a}_i^{(2)}$ is given by:

$$\mathbf{a}_i^{(2)} = \mathbf{a}_{i,0}^{(2)} + \Delta t_{i,0}\mathbf{a}_{i,0}^{(3)} \tag{4.16}$$

In many applications, allowing the time step to change in time can offer a great saving in computational cost, but variable-size time steps usually imply a substantial degradation in energy conservation. Hut et al. (1995) present an algorithm for choosing time steps in such a way as to guarantee time symmetry in any integration scheme, thus allowing vastly improved energy conservation for orbital calculations with variable time steps. The ph4 code in AMUSE applies this algorith to a high order integrator as it is the Hermite scheme.

4.3 The Bridge scheme

The Bridge integrator (Fujii et al., 2007) provides a symplectic mapping for the gravitational evolution in cases were the dynamics of a system can be split into different regimes. The compound nature of the Bridge integrator makes it an ideal target for inclusion within AMUSE, and a generalized Bridge-type gravitational integrator has been implemented in AMUSE. The Bridge formulation can be derived from an Hamiltonian splitting argument; consider the Hamiltonian:

$$H = \sum_{i \in A \cup B} \frac{p_i^2}{2m_i} + \sum_{i \neq j \in A \cup B} \frac{G m_i m_j}{\|r_i - r_j\|}. \tag{4.17}$$

This can be divided into three parts:

$$H = \sum_{i \in A} \frac{p_i^2}{2m_i} + \sum_{i \neq j \in A} \frac{G m_i m_j}{\|r_i - r_j\|} + \sum_{i \in B} \frac{p_i^2}{2m_i} + \sum_{i \neq j \in B} \frac{G m_i m_j}{\|r_i - r_j\|} + \sum_{i \in A, j \in B} \frac{G m_i m_j}{\|r_i - r_j\|} \tag{4.18}$$

$$H = H_A + H_B + H_{A,B}^{int} \tag{4.19}$$

with H_A and H_B the Hamiltonians of subsystems A and B respectively and the cross terms are collected in H^{int}. Now the idea behind the Bridge method becomes more clear, we can perform a time evolution of the system A using a fast tree method and a more accurate time evolution of the system B using a direct method, whereas the interaction is treated as pure momentum kicks. In AMUSE these momentum kicks are computed with a Leapfrog scheme and we can use different codes for treating systems A and B.

4.4 Numerical Setup

The parameters that specify the initial conditions in the simulations are the total gas mass, M_g; the cut-off radius of the gas cloud, R_g; the number of protostars, N; and the average accretion rate, $\dot{m}$. We begin our simulations considering the 6 different accretion scenarios defined in Boekholt et al. (2018), which are based on:

- Finite or infinite gas reservoir, where the second resembles a system that is constantly being fed fresh gas, contrary to the finite gas reservoir models,

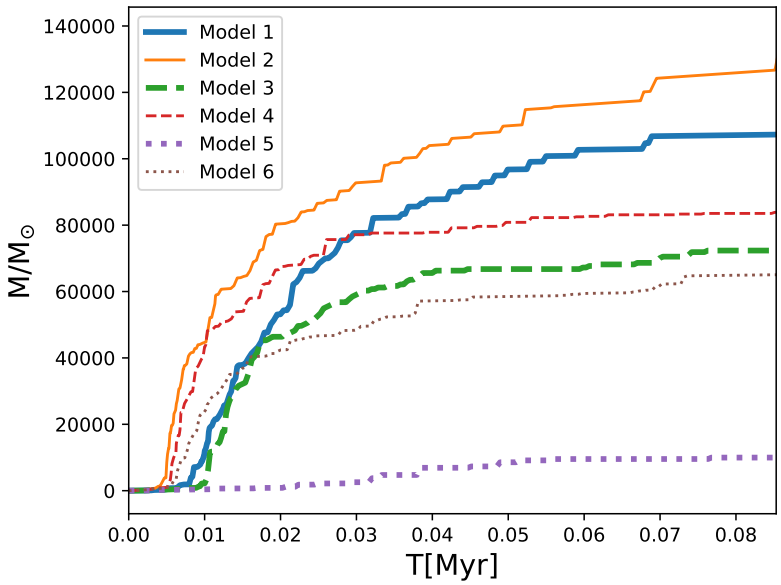

Figure 4.1: Time evolution of the mass of the central object, for six different accretion models. All models, except for number 5, efficiently convert gas mass into one massive object. Here no mass loss is assumed during the collisions.

where we remove the accreted gas from the reservoir, thereby depleting the reservoir. Once it is fully depleted, the accretion rates are set to zero.

- Position dependent accretion rates, that set the accretion rate proportional to the local gas density. In this way the protostars in the core accrete at a higher rate than protostars in the halo.
- Time dependent accretion rates, where we further assume the accretion rate to be proportional to the remaining gas reservoir. We start with the same initial rates, which are decreased as gas is depleted from the reservoir.

The 6 different models are summarized in Table 4.1. Figure 4.1 shows the efficiency of the models on converting the gas mass into one massive object.

We also consider the standard set of parameters used in Boekholt et al. (2018), which are: $M_g = 10^5 M_\odot$, $R_g = 0.1$ pc, $N = 256$, $\dot{m} = 0.03 M_\odot \mathrm{yr}^{-1}$, and mass-radius parametrized tracks based on detailed calculations by Hosokawa et al. (2012), which depend on the accretion rate of the protostar. These tracks are shown in Figure 4.2.

Thus, the radius of a protostar is completely determined by its mass and accretion

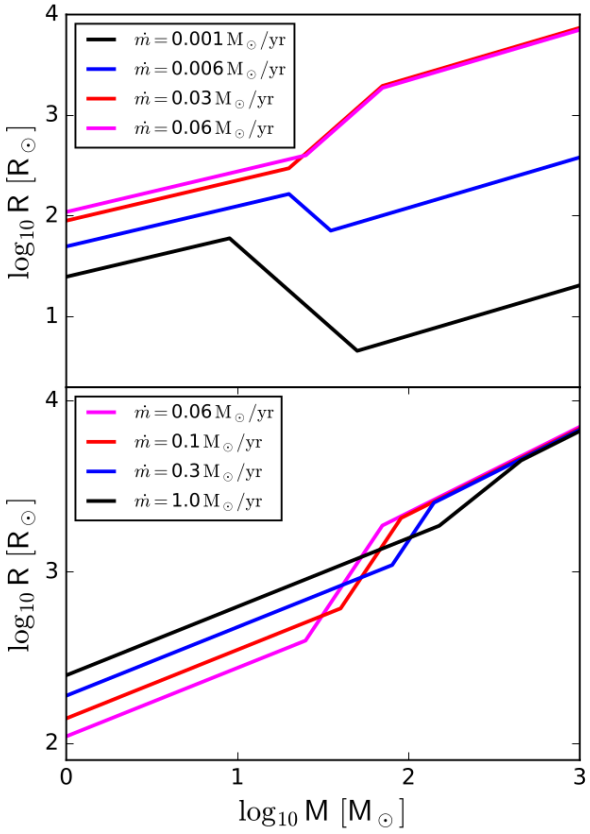

Figure 4.2: Parametrizations of the mass–radius evolution of accreting Pop. III protostars based on Hosokawa et al. (2012). The different colors represent different parametrizations for different accretion rates. Adopted from Boekholt et al. (2018).

Table 4.1: Different accretion models studied.

Model	Gas reservoir	Position dependent accretion model	Time dependent accretion model
1	Infinite	No	No
2	Infinite	Yes	No
3	Finite	No	No
4	Finite	Yes	No
5	Finite	No	Yes
6	Finite	Yes	Yes

rate. At every time-step in the simulation, we keep track of these two quantities and update the radius of the protostar. For values of the accretion rate in between the parametrized mass– radius tracks, we use interpolation between the two nearest tracks in log-space.

The initial mass of the protostars is set to $m_0 = 0.1 M_\odot$ (We note that the mass of the protostar subsequently starts to evolve quickly due to the accretion recipes as well as mergers). This choice of parameter values reflects that we are particularly interested in very massive Pop. III protostar clusters and the formation of very massive objects. We also varied the factor f between 0.85 - 1.00 in steps of 0.01. In order to have good statistics we performed 5 simulations for each value of f per model through models 1, 2, 3, 4 and 6, and 3 simulations for model 5.

As we work with a constant mass loss, we have to consider that in the case of a collision of a very massive object with a light one, the sum of their masses multiplied by a constant factor smaller than 1 could give a final mass smaller than the mass of the most massive collision component. We decided to perform two types of simulations, one that allows for a decrease in the total mass after a collision and also one that just allows for the mass to increase. In the second case, if the mass of the collision product is less than the previous mass, we decided to set the collision product mass equal to the mass of the most massive collision component.

We determine if a simulation is finished by keeping track of the average collision rate

$$\nu_{\rm av}(t) = \frac{N_{\rm col}(t)}{t_{\rm last\ collision}} \tag{4.20}$$

and an upper limit of the current collision rate,

$$\nu(t) = \frac{1}{t - t_{\text{last collision}}}. \tag{4.21}$$

If the ratio of $\nu/\nu_{\text{av}} < 0.015$ we stop the simulation. This criterion was chosen to make sure that most of the collisions have occurred.

4.5 Code adaptation

In this section we describe the modifications made to the collisions code in order to adapt it to our requirements, i.e, including mass loss in stellar collisions. The function that regulates the collisional behavior of the star is called `handle_encounter`, and we have to modify it differently depending on the mass loss scenario that we want.

For constant mass loss

For constant mass loss, our main task is to add a function that changes depending on how much mass we want the stars to lose in each collision. First we sort the index of the stars, so the higher mass star has the primary index. The mass loss input for this function is a factor `k`, which is going to multiply the sum of the masses of the parent stars. In the case that this product is less than the mass of the less massive stars, we adopt the mass of the more massive star to the new star. These implementations can be coded as follows:

```
def handle_encounter(stars, index1, index2, mr_mode,k):
    # Make a CoM particle
    p = Particle()

    p.index = stars[index1].index + "_" +  stars[index2].index
    index_primary = index1
    index_secondary = index2
    if stars[index2].mass > stars[index1].mass:
        index_primary = index2
        index_secondary = index1

    p.mass  = (stars[index1].mass + stars[index2].mass)*k
```

```
    if p.mass < stars[index_primary].mass:
        p.mass = stars[index_primary].mass
```

For the analytic prescription

Now, we want to code the analytic prescription described in Section 3.1, specifically Equations 3.15, 3.16, and 3.17. We start by sorting the index as in the previous modification. Then we calculate the accretion timescale and Kevin-Helmholtz scale for each of the parent stars. Depending on which timescale dominates for each star we will have four scenarios, each one with a different formula for the final mass. The coding is as follows:

```

def handle_encounter(stars, index1, index2, mr_mode):
    # Make a CoM particle
    p = Particle()

    p.index = stars[index1].index + "_" +  stars[index2].index
    index_primary = index1
    index_secondary = index2
    if stars[index2].mass > stars[index1].mass:
        index_primary = index2
        index_secondary = index1

    mdot1 = stars[index1].mdot
    mdot2 = stars[index2].mdot
    M1=stars[index1].mass.value_in(units.MSun)
    R1=stars[index1].radius
    R2=stars[index2].radius
    M2=stars[index2].mass.value_in(units.MSun)
    L1=3.8e4*M1|units.LSun
    L2=3.8e4*M2|units.LSun
    g=constants.G

    tacc1=stars[index1].mass/mdot1
    tacc2=stars[index2].mass/mdot2
    tkh1=g*stars[index1].mass**2/(R1*L1)
    tkh2=g*stars[index2].mass**2/(R2*L2)
    q =stars[index_secondary].mass/stars[index_primary].mass

    if tacc1<tkh1:
```

```
30        if tacc2<tkh2:
31                p.mass  = (stars[index1].mass+stars[index2].mass)
  *(1-0.27*q/(1+q)**2)
32        else:
33            p.mass  = (stars[index1].mass+stars[index2].mass)
  *(1-0.157*(q/(1+q)**2)*(826.92*M1/tkh1+241.11*M2**(0.5))
  /(480.76*M1/tkh1+183.84*M2**(0.5)))
34     else:
35        if tacc2<tkh2:
36           p.mass  = (stars[index1].mass+stars[index2].mass)
  *(1-0.157*(q/(1+q)**2)*(826.92*M2/tkh2+241.11*M1**(0.5))
  /(480.76*M2/tkh2+183.84*M1**(0.5)))
37        else:
38            p.mass  = (stars[index1].mass+stars[index2].mass)
  *(1-0.2059*q/(1+q)**2)
```

After the coding is done, we run the simulations. As they are not expensive, because of the number of particles, we can run them on a standard computer. For the same reason we ran as many as we could to have better results. We have six different accretion models, fifteen different values given to the mass loss factor f, and we ran each scenario five times for statistical purposes, except model five which was ran three times per f value. We did this twice, considering scenarios when the mass of the most massive object could also decrease. In addition, we ran five simulations for each accretion model for the analytical prescription. This adds up for a total of 870 simulations we completed successfully.

Chapter 5

Main Results

The main goal of our simulations is to better understand how the mass of the central object in the cluster changes when mass loss is considered. In the first simulations, we considered constant values for the factor f that regulates mass loss during collisions, and studied how the cluster evolves.

The simulations start with a cluster of single protostars. As the system evolves, different collision products will form due to collisions between the protostars. Also, dynamical encounters among protostars can eject them from the cluster. Thus we define four categories to which a protostar in the simulation can be part of: i) single protostar: which are part of the cluster but are not part of a collision product, ii) the most massive collision product, iii) a less massive collision product, and iv) an escaper: which are stars that are far away from the cluster with positive energy. All the results and methods are described in Alister Seguel et al. (2020).

5.1 Simulations considering constant mass loss

5.1.1 Restricted scenario where mass is only allowed to increase

We first present the results obtained when performing simulations where the mass is only allowed to increase after a collision. In Table 5.1 we show an overview of the results of all the simulations, for all the models studied, in these constant mass loss simulations. The mass loss is described by the value of f, which represents

Table 5.1: Average final masses of the most massive object, obtained in simulations for constant mass loss, where $100f$ is the mass percentage retained per collision. For each model the table shows the average final mass after a simulation, the percentage this mass represents in comparison to the total mass obtained without mass loss, and the σ error for the mass.

	Model 1			Model 2			Model 3		
$100f$	Mass ($M_\odot$)	%	σ	Mass ($M_\odot$)	%	σ	Mass ($M_\odot$)	%	σ
85	22009	20	2773	32290	23	11543	6627	8	1545
86	23731	21	2880	29803	21	6309	7021	9	982
87	23059	20	3406	31503	23	5217	7456	9	969
88	25666	23	1779	32230	23	7701	9209	11	1401
89	25428	23	1779	35371	25	6411	9826	12	1035
90	28942	26	3107	36110	26	2848	11274	14	1885
91	32182	29	2534	41123	30	15663	11586	14	1490
92	29457	26	2536	35436	25	7196	12674	16	1187
93	35107	31	2051	40799	29	2753	13496	17	1711
94	34242	31	4554	45533	33	9741	15921	20	1994
95	37147	33	3169	52715	38	8233	16082	20	1085
96	45838	41	3014	55783	40	5746	17400	22	2013
97	45031	40	5176	52618	38	7082	22053	28	1171
98	59486	54	2912	66223	48	13031	27167	34	1328
99	81334	73	6440	95491	69	5054	39667	50	2165
100	109992	100	8822	136457	100	16177	77962	100	5392

	Model 4			Model 5			Model 6		
$100f$	Mass ($M_\odot$)	%	σ	Mass ($M_\odot$)	%	σ	Mass ($M_\odot$)	%	σ
85	14840	17	1736	2178	16	161	12862	18	1510
86	14927	17	2495	2642	20	370	13652	19	2504
87	15027	17	1867	3479	26	550	16112	23	3814
88	15810	18	2341	3332	25	131	17559	25	975
89	16099	19	2016	3943	30	107	17791	25	1034
90	17651	20	1131	3429	26	1387	16561	24	2048
91	19384	22	1669	4439	34	426	18374	26	2725
92	19912	23	1362	4186	32	520	18982	27	1885
93	21854	25	2613	5157	39	242	21958	32	1311
94	23655	27	1813	5092	39	1095	20362	29	1650
95	26838	31	3160	6621	51	464	24351	35	3623
96	28448	33	837	8287	64	670	25074	36	3173
97	32457	38	1224	7515	58	127	28820	42	3246
98	38402	45	1601	8971	69	845	32367	47	2203
99	51641	60	1089	11760	90	1262	45806	66	1125
100	84671	100	4570	12925	100	2214	68615	100	3477

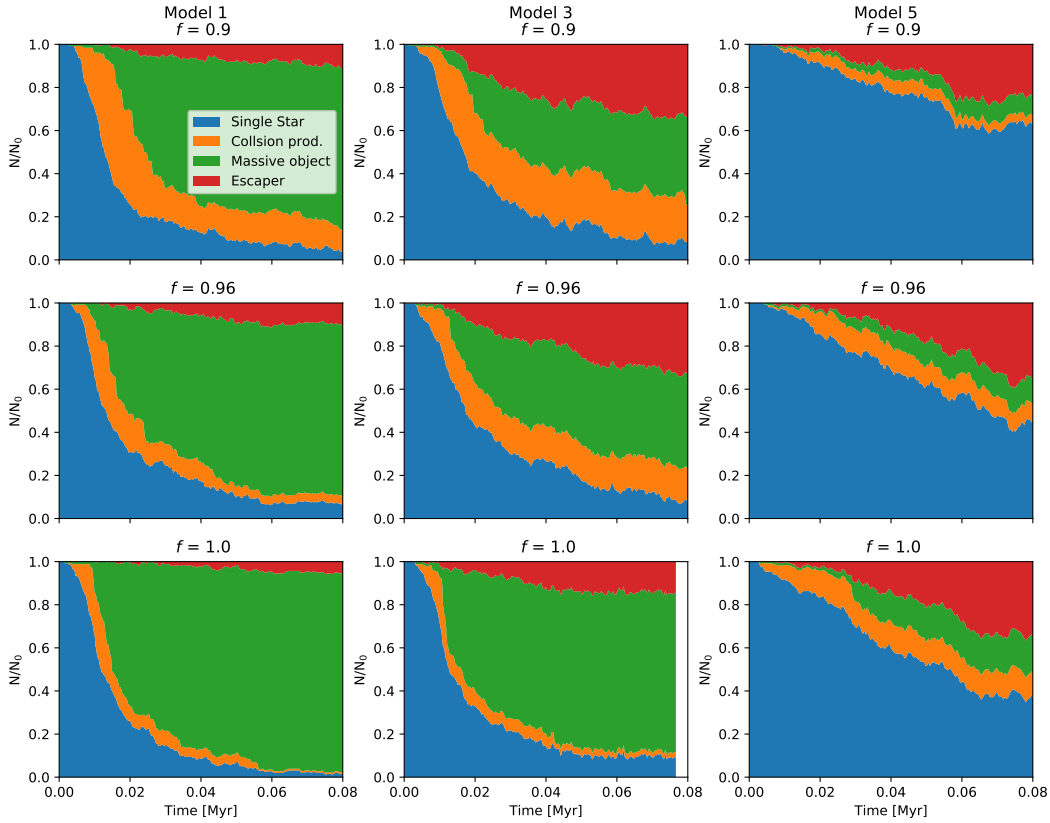

Figure 5.1: Fraction of stars over time corresponding to four categories: escapers (red); stars that have collided with and are part of the most massive star in the system (green, 'Massive object'); stars that are part of other collision products (orange, 'Collision prod.'); and single stars (blue), for different models, and different values for the fraction of mass conserved after a collision f. The general trend for the models is that the fraction of stars being part of the most massive object decreases when f decreases. Adopted from Alister Seguel et al. (2020).

the fraction of mass that remains after a collision. The table shows the value of the average final mass for the most massive object at the end of the simulation from multiple random realisations, the percentage that the mass represents in comparison to the final mass when no mass loss is considered, and the standard deviation σ for the mass, considering a set of five simulations for every model, except for model five with just three simulations.

We also present the time evolution of the fraction of protostars belonging to each of the previously defined categories in Figure 5.1 in a single simulation, for the position independent models (1, 3 and 5), which are representative for the different

kind of behaviours seen on our models. When $f = 1$ (i.e. there is no mass loss), the majority of protostars end up in the final most massive object for models 1 and 3, while most of the stars do not undergo merger events in model 5. In the first models, as a result of gas accretion, the protostars are growing in radius, because protostellar mass and accretion rates are also increasing, thus getting a larger cross-section, resulting in a high collision probability in this environment. As we decrease the value of f, the fraction of objects that become part of the most massive object decreases, but the number of protostars that escape, or take part in a less massive collision product increases, as a result of the lower gravitational potential at the center of the cluster, due to less mass in that area. In model 5, because of the uniform accretion, the central object in this model is less massive, and due to the time-dependent accretion, the protostellar radii shrink again as the cluster runs out of gas. We observe that most of the stars remain single, and we see a higher fraction of escapers than in the other models; as we decrease f, the fraction of single stars becomes higher while the other fractions decrease.

Figures 5.2, 5.3, and 5.4, present the collision rate (bottom panels) in a single simulation, and correlate it with the total star and gas mass (top panels), the fraction of stars belonging to the four categories defined earlier (second panels), and the radius of the most massive protostar and the average radius of all the remaining protostars (third panels), where the average radius is the number averaged radius of all stars except the most massive one, for the three position independent models 1, 3, and 5, using $f = 0.9$, 0.96 and 1. In every model the collision rate starts to increase rapidly on a timescale of the order of 10^4 years after the simulation has begun, which is short compared to the total duration of the simulation. This timescale corresponds to the time it takes for the protostars to gain mass and obtain a larger radius, and also for the total stellar mass to be comparable to the gas mass. After reaching its peak, the collision rate decreases steadily and a small amount of objects starts to escape. The protostars grow rapidly and make the system stellar-mass dominated, producing dynamical encounters and collisions. For model 1 we find that the stars have a tendency to form a massive central object, with a low rate of escapers through the simulation, and as model 3 presents an equally efficient way to form a massive object, the rate of escapers is higher, especially at later times. Model 5 forms an object of moderate mass of $\sim 4000 M_{\odot}$, and presents a steady escape rate.

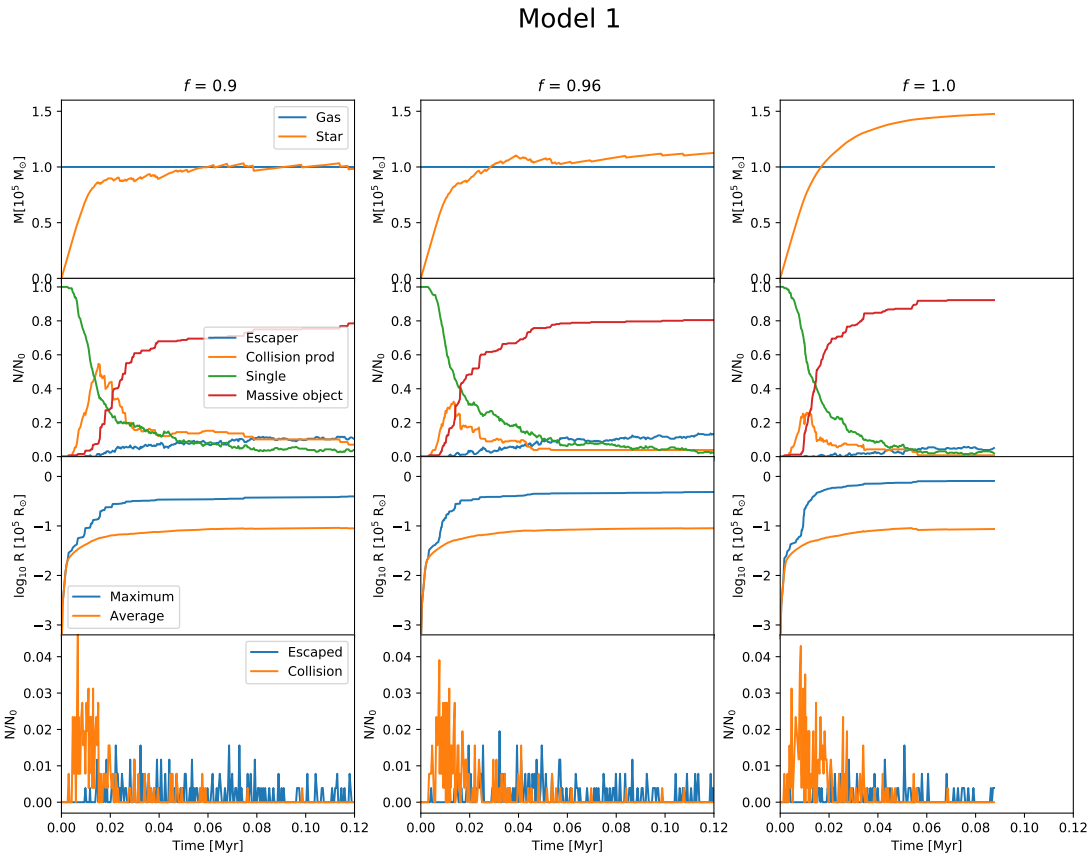

Figure 5.2: Correlation of the time evolution of the collision and escape rate (bottom panel) with: total star and gas mass (top panel), fraction of stars belonging to the same four categories as in Fig. 5.1 (second panel), and maximum stellar radius and average stellar radius of the remaining stars (third panel), for three different and representative values of the retained mass fraction f. Adopted from Alister Seguel et al. (2020).

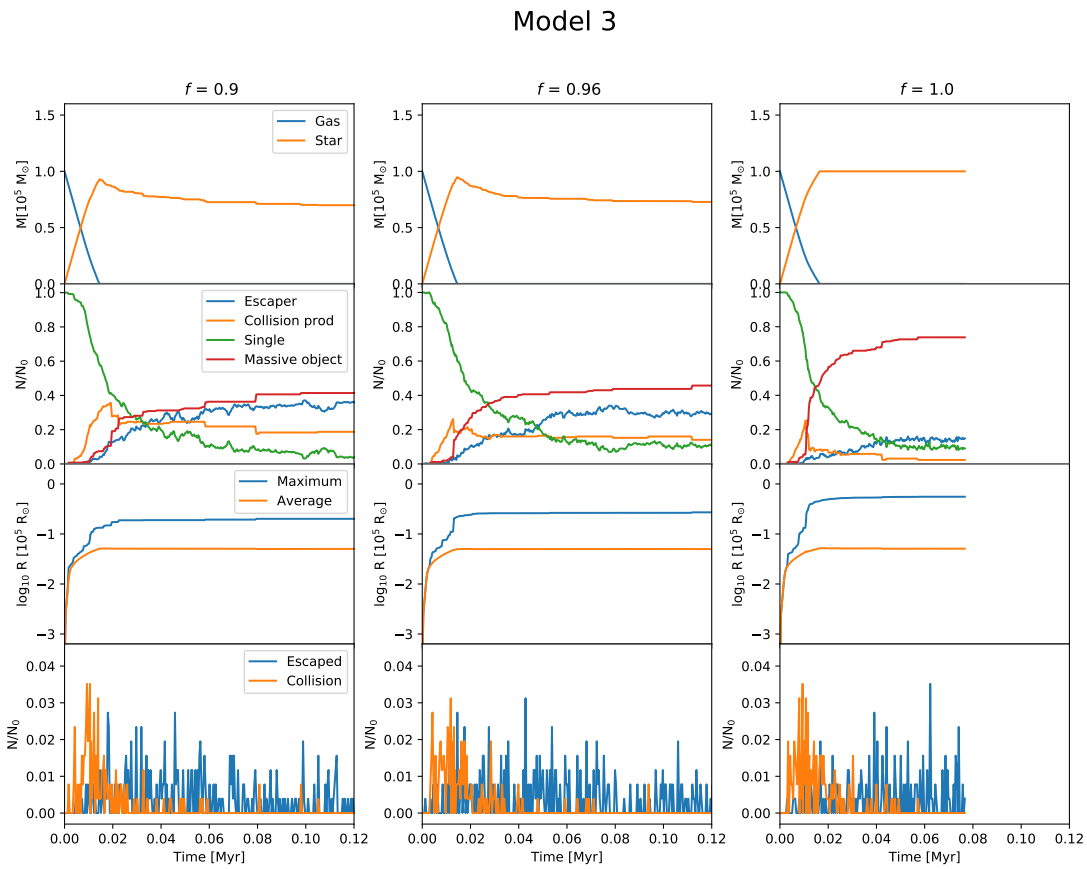

Figure 5.3: Same as Fig. 5.2 for model 3. Adopted from Alister Seguel et al. (2020).

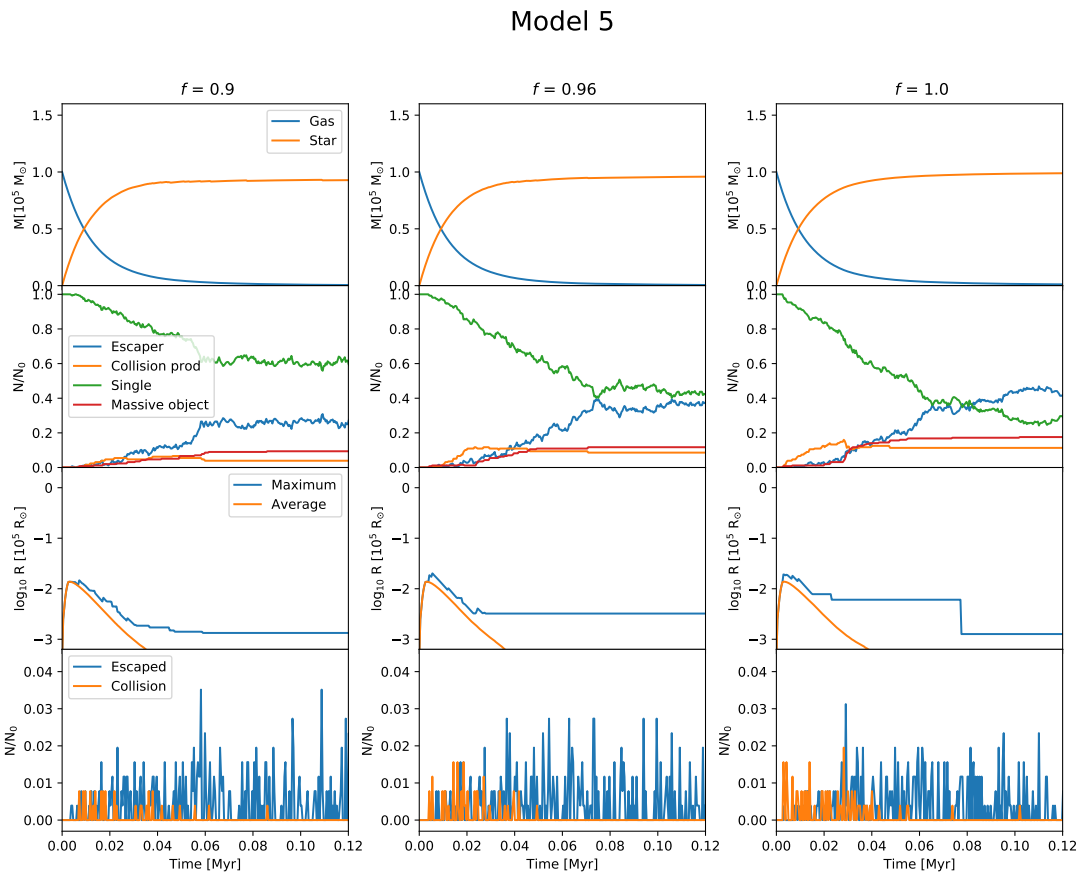

Figure 5.4: Same as Fig. 5.2 for model 5. Adopted from Alister Seguel et al. (2020).

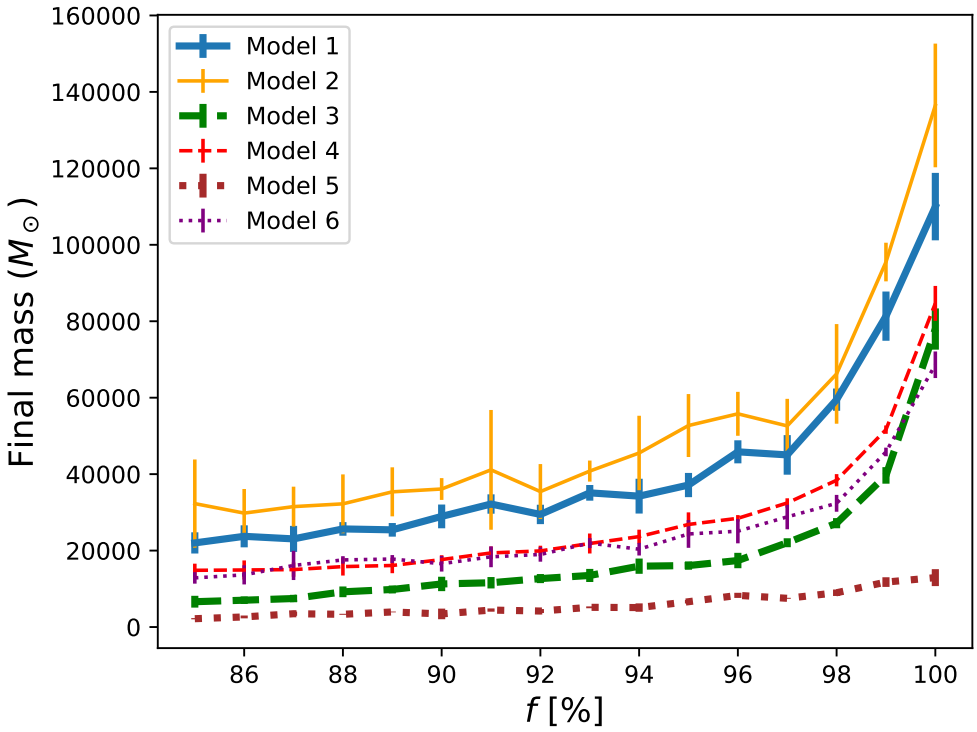

Figure 5.5: Final mass of the most massive object at the end of each simulation, as a function of the retained mass fraction f, for each model described. The bar at each point simulated represents the σ error considering 5 simulations for each f per model. Adopted from Alister Seguel et al. (2020).

The comparison between the scenarios with different values of f is clear. A lower value of f corresponds to a lower value in the total stellar mass of the system, and a lower fraction of the number of stars that form the most massive object in the cluster, also increasing the number of objects that escape. The average radius of the stars does not seem to be affected, but it is clear that the radius of the most massive object also decreases with f. The biggest difference is between f values of 0.96 and 1. For 0.9 and 0.96, while there are differences, they are more subtle and not as important, which suggests that between this range of higher mass loss the simulations evolve in a similar way, so changing the value of f is not as fundamental in this regime.

Now, to understand the effect on the final mass of the central object, we show the final mass as a function of f in Figure 5.5, for all the simulations we performed in a scenario where the mass is restricted to only grow. We find that for models

1 and 2 the behaviour of the curve changes abruptly when f reaches a value of ~ 0.96, for models 3, 4 and 6 there is also a sudden change of behaviour around the same value, but not as steep as the first one, while model 5 does not present this abrupt change. It is easy to see that there is a steep dependence on f in the interval $f = [0.96 - 1.00]$, where the mass of the final object changes steeply with the precise value of f, so that even a small mass loss fraction is still relevant, obtaining values of almost one third of the mass obtained in simulations where mass loss is not considered. On the other hand, in the range $f = [0.85, 0.96]$, changes in the value of f do not lead to a big change in the final mass obtained. This suggests that when considering a constant mass loss per collision, there is a breaking point where the mass loss fraction is a deciding factor in the resulting final mass of the most massive object. For high values of f, the growth of the mass is dominated by collisions, and for lower values, it is dominated by accretion, explaining why at these lower values a change in mass loss is not as relevant. Here, as mass has a direct effect on the cross section and gravitational potential of the protostars, there would not be as many collision as if f where higher (which represent more massive stars), thus explaining the change of behaviour. It also explains why model 5 is not as affected with the f changes, as this model is the most conservative and few collisions take place.

Another point to consider when reaching values of f of ~ 0.96, is that the typical masses of the protostars, around the final stages when they collide, are between $500 - 1000 M_{\odot}$, while the central object has a mass of the order of several $10^5 M\odot$, therefore the mass loss is comparable to the mass gain during the collision, reducing the net effect. Considering the accretion rate, mass increases by about $300 M\odot$ in 0.01 Myr, so for this range of values of f the mass loss during collisions with the massive object becomes comparable to the mass that has previously been accreted. This adds up to the previously stated circumstances where for lower values of f the growth of the mass is not dictated by collisions, but by the accretion rate of the protostars.

5.1.2 Unrestricted scenario where mass is also allowed to decrease

Our second scenario for constant mass loss is one where the total mass of colliding objects is allowed to decrease after a collision. We performed the same type

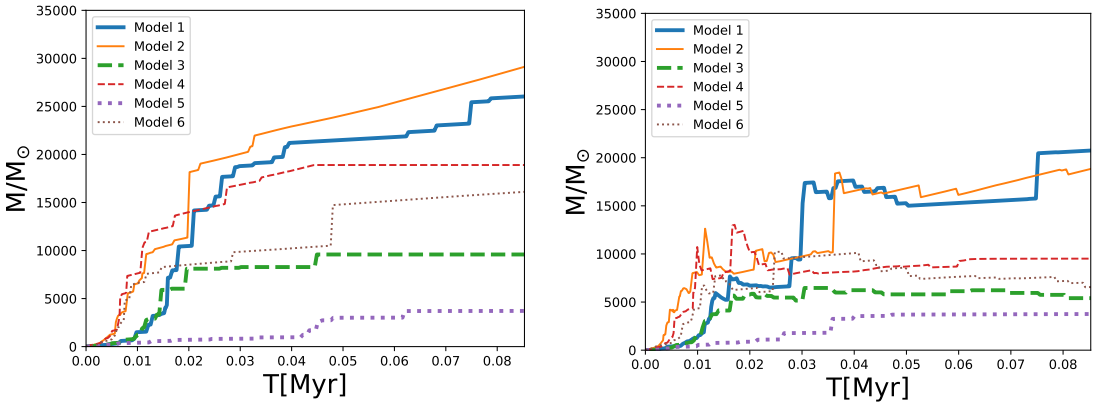

(a) Restricted **(b)** Unrestricted

Figure 5.6: Time evolution of the mass of the central object, for six different accretion models considering a 10% mass loss per collision. On the left we show a restricted model (a) which only allows mass to increase, and on the right an unrestricted model which allows mass to decrease after a collision. All models, except for number 5, efficiently convert gas mass into one massive object. Adopted from Alister Seguel et al. (2020).

of simulations as in the previous case, and then decided to compare both of them directly. Our first comparison was between the efficiency of the models to produce a massive object on a given timescale, for a given value of f. We used a value of 0.9 (i.e. a mass loss of 10% per collision), as this represents a lower limit in the literature, and it is a considerable amount of mass loss in any case. Figure 5.6 shows the growth of the most massive object for a restricted and an unrestricted scenario, demonstrating that when allowing for the mass to decrease after a collision, the efficiency to create a massive object decreases. Considering that sooner or later the central object would collide with low mass objects, this decrease was to be expected. Despite this, the unrestricted model still is able to create very massive objects on the given timescale. This mass is not the total mass of the central object obtained at the end of the simulation, but gives us insight on what we could expect, given the initial efficiency to create a massive object, and that the number of collisions over time has already reached its peak.

Now we can show the how the value of f affects the final mass of the central object in this scenario, and how this value differs from the previous case. For that, we compare the final mass obtained in the restricted and unrestricted scenarios as a function of f , for each model separately, in Figure 5.7. The first thing to

note is that they follow the same global behaviour, there is a step dependence on the f value in the f interval [0.96-1], while for lower f values a change in f does not affect significantly the final mass obtained. Naturally, when f approaches 1 the mass we are going to obtain is the same as if we do not consider mass loss at all in the simulations, regardless of the kind of scenario we are in, restricted or unrestricted, so it is to be expected that both types of simulations behave the same at high f values. Contrasting the mass difference for these high values of f between the models we note that it is almost negligible, for all the models. In particular, we note that in models 1 and 3 there is very little difference between restricted and unrestricted case, across all the values of f tested, while in models 2, 4 and 6 the difference between these scenarios is more notorious for values of f lower than 0.96. Model 3 exhibits a more erratic behaviour at higher f values, but the masses obtained for both models are in the same range.

These results tells us that in the range where changes in f are crucial (i.e. f in the range 0.96-1), the results do not sensitively depend on the type of scenario, restricted or unrestricted. As for lower values of f, there are distinguishable differences, particularly for position dependent accretion models, where the mass in the unrestricted case can be as half as much of the restricted one as that in this regime. This could be explained by the fact that the unfrequent collisions may even remove some of the gas that has been accreted before.

5.2 Simulations considering the analytical prescriptions

Lastly, we performed simulations using the mass loss parametrizations from Glebbeek and Pols (2008) (Equation 3.2), and Lombardi et al. (2002) (Equation 3.1) combined with the Schleicher et al. (2013) mass-radius relationship (Equation 3.3). Equation 3.2 presented us a simple prescription for mass loss, where the f domain is limited, as shown in Figure 5.8, where is clear that in this prescription the mass loss per collisions will never exceed an 8%. Equations 3.15, 3.16, and 3.17 presented us four different cases for mass loss depending on the parent star. For each model we performed five simulations using these parametrizations, while for model five we just performed three. The final mass averages obtained after these simulations are given by Table 5.2, where we also show the projected f value

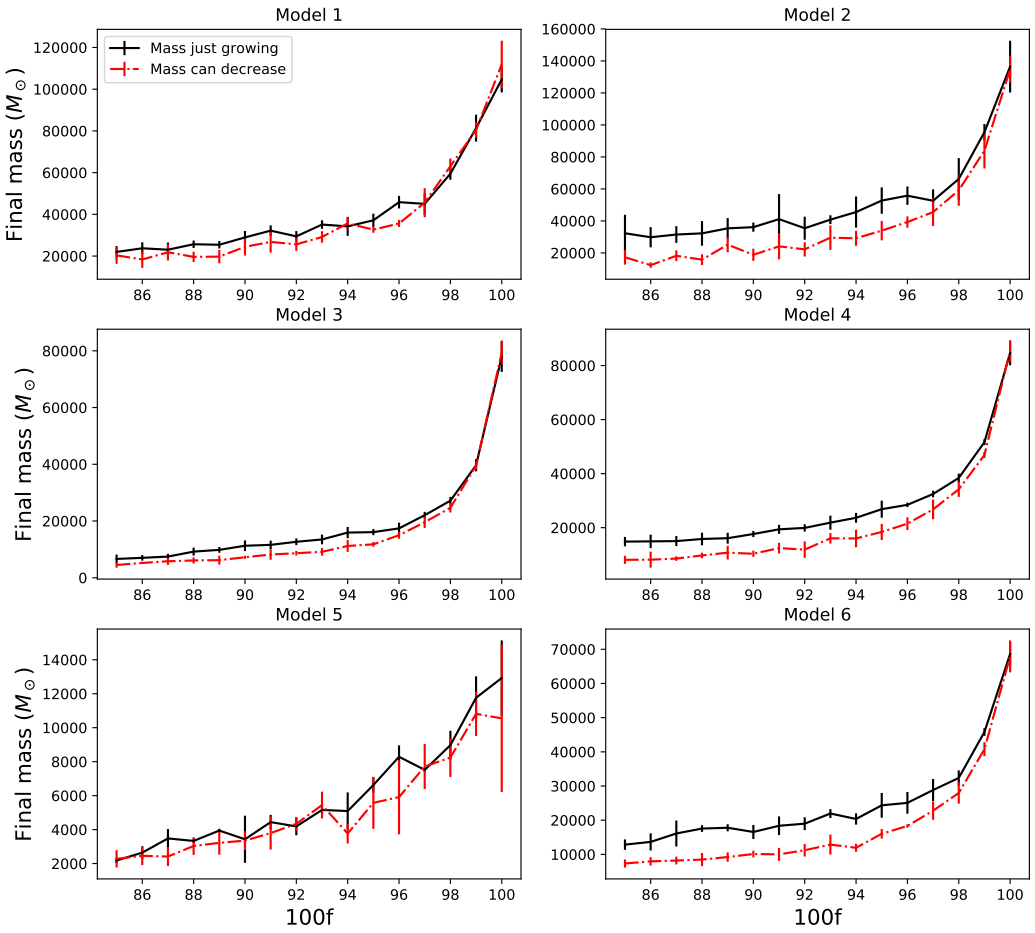

Figure 5.7: Comparison of models where the mass of the most massive object can only increase (black line) after a collision, and models that allow a decreasing mass (red). Each point in each plot has a bar representing the σ error considering 5 simulations for each retained mass fraction f per model. Adopted from Alister Seguel et al. (2020).

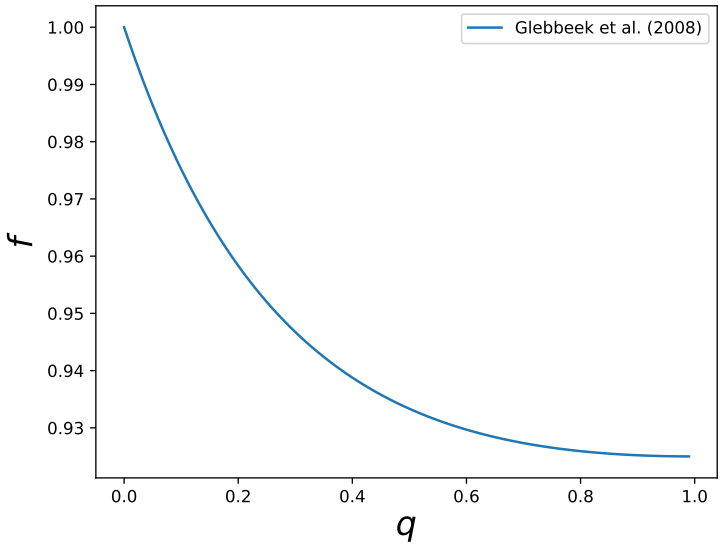

Figure 5.8: Dependence of f on the mass ratio q, for the Equation 3.2 from Glebbeek and Pols (2008). For all possible q values, the value of f never gets below 0.92

that would have corresponded to that final mass in a constant mass per collision scenario, the mass percentage of the final mass in relation to a scenario without mass loss, and the σ error per model and prescription.

The average final masses obtained are compared with the final masses of a constant mass loss restricted scenario. It shows that we can consider the prescriptions to be equivalent to a certain constant mass loss scenario. Fig. 5.9 shows the results we get for both prescriptions used, compared with the result we previously had in the constant mass loss scenario, for each accretion model separately. In general, the trend is that the prescriptions can be compared to a constant mass loss configuration where $f \sim 0.99$, nonetheless, the exact value depends on the accretion model we consider. We also note that the parametrization using the Schleicher et al. (2013) protostellar models gives slightly higher values for the final mass than the simpler prescription by Glebbeek and Pols (2008), and the dispersion between them depends also on the accretion model we consider. In most of the simulations, the central object will collide with objects much less massive, making the mass ratio q smaller, thus giving lower values for the mass loss. This explains why for the parametrizations used the final mass obtained can be compared with a high f constant mass loss scenario, as in both cases the mass loss are low.

Table 5.2: Overview of the results of the simulations using the mass loss prescriptions by Glebbeek and Pols (2008), and Lombardi et al. (2002) combined with Schleicher et al. (2013) mass-radius relationship for protostars. We including the average final mass, projected f value which corresponds to that final mass in a constant mass loss scenario, percentage of the total mass compared to a scenario without mass loss, and the standard deviation σ for each set of simulations.

	Glebbeek				Lombardi - Schleicher			
Model	Mass ($M_\odot$)	f	%	σ	Mass ($M_\odot$)	f	%	σ
1	78003	98.84	74	3148	89151	99.33	85	6041
2	96714	99.03	70	13035	109889	99.35	80	6465
3	42214	99.06	54	6361	51240	99.30	65	3195
4	55610	99.12	65	2370	63185	99.34	74	2356
5	7683	97.11	59	1678	8737	97.83	67	920
6	46980	99.5	68	3135	55595	99.42	81	2752

In general, for all the mass loss scenarios studied, constant mass loss and mass loss dictated by prescriptions, we can obtain masses of the order of $10^4 M_\odot$ and higher, except for model five for specific, extreme f values. These results are compatible with the mass that SMBH seed need to grow into the high redshift SMBHs we see today.

As the parametrizations used are modeled after collision of main sequence stars, a possibility to consider is that they underestimate the real mass loss between a collision of protostars, considering that fundamental properties, such larger cross sections, or weakly bounded envelops, that could affect the merging between two of these objects. Further studies in protostar collisions will provide more detailed answers.

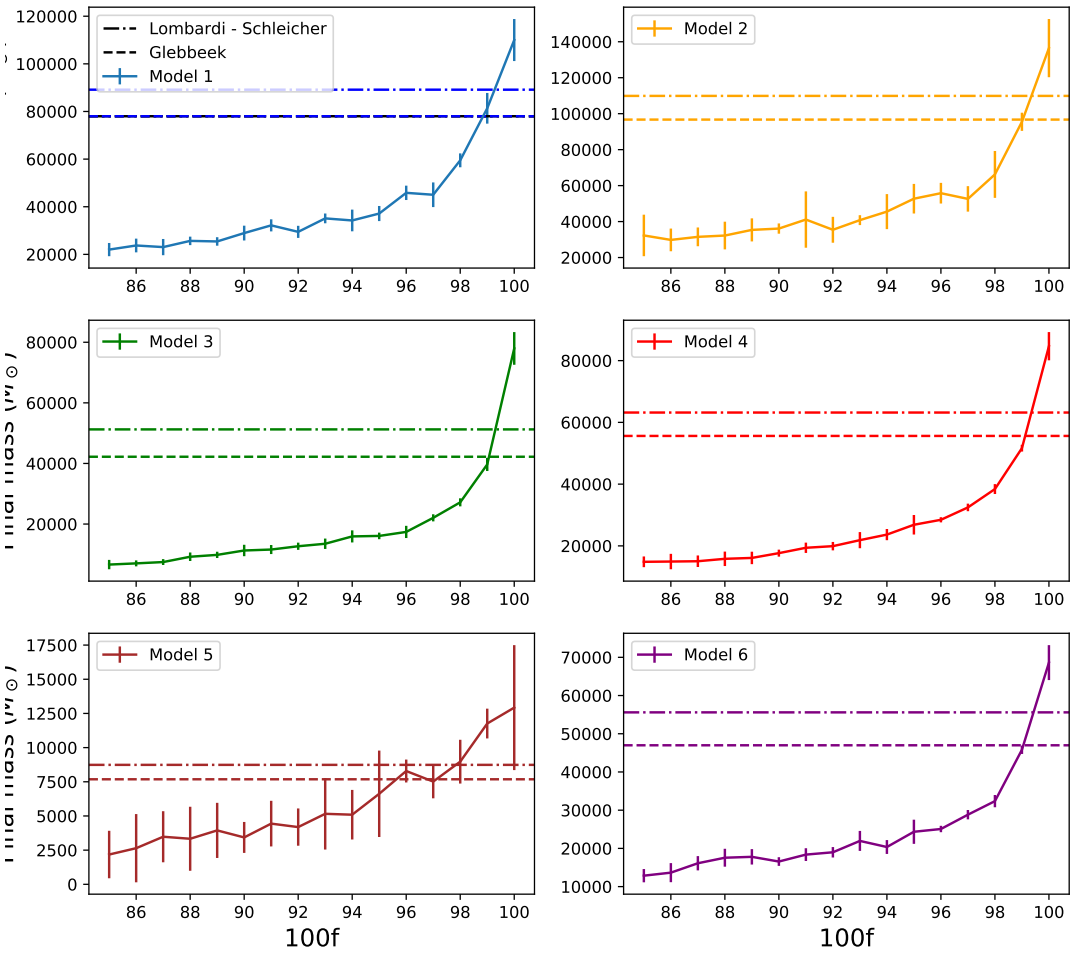

Figure 5.9: Results of simulations using the mass loss prescriptions by Glebbeek and Pols (2008), and Lombardi et al. (2002) combined with Schleicher et al. (2013) mass-radius relationship for protostars. These results are compared with the restricted constant mass loss scenario. The dashed line in each plot represents the simpler prescription given by Equation 3.2, meanwhile the dash-dotted line represents the results of the more complex parametrization given by Equation 3.1 .Each line represents the mean of final mass for 5 simulations. Adopted from Alister Seguel et al. (2020).

Chapter 6

Summary and Conclusions

We have presented a study of how the mass loss during collisions can affect the final mass during the formation of SMBH seeds, formed through collisions and accretion, in a dense, primordial Pop. III protostellar cluster. We take into account standard cluster parameters as introduced by Boekholt et al. (2018), which ensure the production of massive black hole seeds. We investigated the effect of mass loss by a constant fraction of the told mass per collision. We perform a series of simulations using the AMUSE framework, which included N-body dynamics, an analytical gas potential, different accretion models, mass-radius parametrizations, and stellar collisions.

Investigations on mass loss in collisions of stars provide information how much mass loss we could expect between certain kind of stars, but protostellar collisions have not been explored yet.

In our work, we first present the time evolution of the stellar components of the cluster for our representative accretion models in Figure 5.1, which shows that for higher mass loss, the fraction of stars which become part of the most massive object decreases, while the single stars and escaper fraction gets larger, due to the fact that the cluster gravitational potential becomes smaller when mass loss increases. Our results can be summarized as follows:

- We present the results of our first simulations in Figure 5.5 , which shows the dependence of the final mass of the most massive object with the factor f that describes mass loss. We can clearly see two distinct behaviors, for higher values of f the mass depends steeply on its value, while for lower

values the final mass does not change much with f, this can be explained because at the higher end of the plot the growth of the mass is dominated by collisions, and accretion dominates for the lower end.

- When comparing the previous scenario with scenarios that allow for a decrease, in Figure 5.7 we see that the differences between scenarios are more significant for lower values of f, while for higher values there is not much difference. This shows that in the range where changes in f are important, whether or not we allow for the mass of an object to decrease after a collision is not really relevant. In this context, a constant mass loss of 5% represents a final mass between 60-80% lower (50% for model 5) than the mass we would get if we did not consider mass loss in our models.

- Also, comparing the results of the constant mass loss simulations with more complex mass loss parametrizations by Lombardi et al. (2002) and Glebbeek and Pols (2008), using the Schleicher et al. (2013) mass-radius relationships for primordial protostars gives us different results. The obtained results tell us that these analytical models are equivalent to scenarios of constant mass loss of ∼1% per collision. However, this low mass loss percentage can have a great impact on the final mass of the object, that could lose between 15 to 40% of its mass depending on the accretion model we study.

6.1 Discussion

Our investigation gave insight on the effect of mass loss during collisions, in the formation of a possibly SMBH seed. We used simplified models for the mass loss and analytical models in the literature by Lombardi et al. (2002) and Glebbeek and Pols (2008). These models are limited, first, in the sense that a constant fraction of mass loss for every collisions is not the most realistic approach, as mass loss is affected by the properties of the stars themselves, such as the relative velocity at the moment of the collision, and the position of the stars relative to another, or their masses and evolutionary stage, so a constant mass loss scenario is very simplified. The analytical prescriptions that we used were shown to work well for main-sequence stars, but they could potentially underestimate the mass loss in protostars, as the properties between these two kind of stars are different. Despite these limitations, we were able to get final masses of the order of $10^4 M_\odot$,

which can be considered massive enough to be SMBH seeds, even in the most extreme scenarios. We can conclude that mass loss plays an important role on the final mass of the object formed, but despite this, the runaway collision model we explored is still a strong candidate for explaining the SMBHs we see nowadays.

There is still ongoing research on the formation and evolution of primordial dense clusters. Our cluster model was simplified, as we did not assume any initial mass function, and it adopts the Plummer sphere distribution for the stars, and for the gas. In order to obtain the most accurate results it is also important to improve the current models. An initial mass function may trigger a mass segregation that would favour the formation of more massive objects, but lead to more ejected stars, particularly if they are not as massive.

The mass loss in collisions of primordial protostars has not been studied, and given the influence of mass loss in the context of the formation of SMBH seeds, it is important to explore this in more detail in the future, via hydrodynamical simulations, considering also three-body mergers and different relative velocities, with the aim to derive approximate relations that can subsequently be employed in accurate N-body models. Despite not knowing some characteristics of the primordial stars clusters, there is ongoing research dedicated to better understand the early evolution of the first star clusters and the formation of massive objects in their center. The runaway collision scenario is promising for the formation of very massive objects, and new models will shed more light on the formation processes of SMBHs.

Bibliography

Agarwal, B., Cullen, F., Khochfar, S., Klessen, R. S., Glover, S. C. O., and Johnson, J. (2017). Effects of binary stellar populations on direct collapse black hole formation. *MNRAS*, 468(1):L82–L86.

Agarwal, B. and Khochfar, S. (2014). Revised rate coefficients for H2 and H-destruction by realistic stellar spectra. *MNRAS*, 446(1):160–168.

Alister Seguel, P. J., Schleicher, D. R. G., Boekholt, T. C. N., Fellhauer, M., and Klessen, R. S. (2020). Formation of SMBH seeds in Population III star clusters through collisions: the importance of mass loss. *Monthly Notices of the Royal Astronomical Society*, 493(2):2352–2362.

Bañados, E. et al. (2018). An 800-million-solar-mass black hole in a significantly neutral universe at a redshift of 7.5. *Nature*, 553:473.

Baumgardt, H. and Klessen, R. S. (2011). The role of stellar collisions for the formation of massive stars. *Monthly Notices of the Royal Astronomical Society*, 413(3):1810–1818.

Boehle, A., Ghez, A. M., Schödel, R., Meyer, L., Yelda, S., Albers, S., Martinez, G. D., Becklin, E. E., Do, T., Lu, J. R., and et al. (2016). An improved distance and mass estimate for sgr a* from a multistar orbit analysis. *The Astrophysical Journal*, 830(1):17.

Boekholt, T., C. N. et al. (2018). Formation of massive seed black holes via collisions and accretion. *MNRAS*, 476:366.

Bovino, S., Grassi, T., Schleicher, D., R. G., and Banerjee, R. (2016). The formation of the primitive star sdss j102915+172927: Effect of the dust mass and the grain-size distribution. *ApJ*, 832:154.

Bovino, S., Grassi, T., Schleicher, D., R. G., and Latif, M., A. (2014). Formation of carbon-enhanced metal-poor stars in the presence of far-ultraviolet radiation. *ApJL*, 790:L35.

Bromm, V. and Loeb, A. (2003). Formation of the first supermassive black holes. *ApJ*, 596:34.

Chandrasekhar, S. (1964). The dynamical instability of gaseous masses approaching the schwarzschild limit in general relativity. *The Astrophysical Journal*, 140:417.

Dale, J. E. and Davies, M. B. (2006). Collisions and close encounters involving massive main-sequence stars. *MNRAS*, 366(4):1424–1436.

Devecchi, B. and Volonteri, M. (2009). Formation of the first nuclear clusters and massive black holes at high redshift. *ApJ*, 694:302.

Dijkstra, M., Ferrara, A., and Mesinger, A. (2014). Feedback-regulated supermassive black hole seed formation. *MNRAS*, 442(3):2036–2047.

Dopcke, G., Glover, S., C. O., Clark, P., C., and Klessen, R., S. (2013). On the initial mass function of low-metallicity stars: The importance of dust cooling. *ApJ*, 766:103.

Espinoza, P., Selman, F. J., and Melnick, J. (2009). The massive star initial mass function of the arches cluster ***. *A&A*, 501(2):563–583.

Fujii, M., Iwasawa, M., Funato, Y., and Makino, J. (2007). BRIDGE: A Direct-Tree Hybrid
N
-Body Algorithm for Fully Self-Consistent Simulations of Star Clusters and Their Parent Galaxies. *PASJ*, 59(6):1095–1106.

Gaburov, E., Lombardi, J. C., J., and Portegies Zwart, S. (2008). Mixing in massive stellar mergers. *MNRAS*, 383(1):L5–L9.

Gaburov, E., Lombardi, J. C., and Zwart, S. P. (2010). On the onset of runaway stellar collisions in dense star clusters – II. Hydrodynamics of three-body interactions. *MNRAS*, 402(1):105–126.

Glebbeek, E., Gaburov, E., de Mink, S. E., Pols, O. R., and Portegies Zwart, S. F. (2009). The evolution of runaway stellar collision products. *A&A*, 497(1):255–264.

Glebbeek, E., Gaburov, E., Portegies Zwart, S., and Pols, O. R. (2013). Structure and evolution of high-mass stellar mergers. *Monthly Notices of the Royal Astronomical Society*, 434(4):3497–3510.

Glebbeek, E. and Pols, O. R. (2008). Evolution of stellar collision products in open clusters * - ii. a grid of low-mass collisions. *A&A*, 488(3):1017–1025.

Heger, A., Fryer, C. L., Woosley, S. E., Langer, N., and Hartmann, D. H. (2003). How massive single stars end their life. *The Astrophysical Journal*, 591(1):288–300.

Hirano, S., Hosokawa, T., Yoshida, N., Omukai, K., and Yorke, H. W. (2015). Primordial star formation under the influence of far ultraviolet radiation: 1540 cosmological haloes and the stellar mass distribution. *Monthly Notices of the Royal Astronomical Society*, 448(1):568–587.

Hosokawa, T. and Omukai, K. (2009). Evolution of massive protostars with high accretion rates. *The Astrophysical Journal*, 691(1):823–846.

Hosokawa, T., Omukai, K., and Yorke, H., W. (2012). Rapidly accreting supergiant protostars: Embryos of supermassive black holes? *ApJ*, 756:93.

Hut, P., Makino, J., and McMillan, S. (1995). Building a Better Leapfrog. *The Astrophysical Journal*, 443:L93.

Katz, H., Sijacki, D., and Haehnelt, M. G. (2015). Seeding high-redshift QSOs by collisional runaway in primordial star clusters. *MNRAS*, 451(3):2352–2369.

Latif, M., A., Bovino, S., Grassi, T., Schleicher, D., R. G., and Spaans, M. (2015). How realistic UV spectra and X-rays suppress the abundance of direct collapse black holes. *MNRAS*, 446:3163.

Latif, M. A., Schleicher, D. R. G., Bovino, S., Grassi, T., and Spaans, M. (2014). The formation of massive primordial stars in the presence of moderate uv backgrounds. *ApJ*, 792(1):78.

Latif, M. A., Schleicher, D. R. G., Schmidt, W., and Niemeyer, J. (2013). Black hole formation in the early universe. *MNRAS*, 433(2):1607–1618.

Loeb, A. and Rasio, F. A. (1994). Collapse of Primordial Gas Clouds and the Formation of Quasar Black Holes. *ApJ*, 432:52.

Lombardi, Jr., J. C., Warren, J. S., Rasio, F. A., Sills, A., and Warren, A. R. (2002). Stellar collisions and the interior structure of blue stragglers. *ApJ*, 568(2):939–953.

Magorrian, J., Tremaine, S., Richstone, D., Bender, R., Bower, G., Dressler, A., Faber, S. M., Gebhardt, K., Green, R., Grillmair, C., Kormendy, J., and Lauer, T. (1998). The demography of massive dark objects in galaxy centers. *The Astronomical Journal*, 115(6):2285–2305.

Mayer, L., Latif, M., and Schleicher, D., R. G. (2013). Super-eddington accretion; flow regimes and conditions in high-z galaxies. *Formation of the First Black Holes*, pages 195–228.

McConnell, N. J. and Ma, C.-P. (2013). REVISITING THE SCALING RELATIONS OF BLACK HOLE MASSES AND HOST GALAXY PROPERTIES. *The Astrophysical Journal*, 764(2):184.

Mehrgan, K., Thomas, J., Saglia, R., Mazzalay, X., Erwin, P., Bender, R., Kluge, M., and Fabricius, M. (2019). A 40-billion solar mass black hole in the extreme core of Holm 15A, the central galaxy of Abell 85. *arXiv e-prints*, page arXiv:1907.10608.

Mortlock, D. J., Warren, S. J., Venemans, B. P., Patel, M., Hewett, P. C., McMahon, R. G., Simpson, C., Theuns, T., Gonzáles-Solares, E. A., Adamson, A., and et al. (2011). A luminous quasar at a redshift of z = 7.085. *Nature*, 474(7353):616–619.

Omukai, K., Schneider, R., and Haiman, Z. (2008). Can supermassive black holes form in metal-enriched high-redshift protogalaxies? *ApJ*, 686:801.

Pelupessy, F., I., van Elteren, A., de Vries, N., McMillan, S. L. W., Drost, N., and Portegies Zwart, S. F. (2013). The astrophysical multipurpose software environment. *A&A*, 557:A84.

Portegies Zwart, S., F. et al. (2009). A multiphysics and multiscale software environment for modeling astrophysical systems. *New Astron.*, 14:369.

Portegies Zwart, S. and McMillan, S. (2018). *Astrophysical Recipes; The art of AMUSE*. IOP Publishing.

Portegies Zwart, S., McMillan, S., van Elteren, A., Pelupessy, F., and de Vries, N. (2013). Multi-physics simulations using a hierarchical interchangeable software interface. *Comput. Phys. Com.*, 184:456.

Rees, M., J. (1984). Black hole models for active galactic nuclei. *ARA&A*, 22:471.

Reinoso, B., Schleicher, D., Fellhauer, M., Klessen, R., and Boekholt, T., C. N. (2018). Collisions in primordial star clusters - formation pathway for intermediate mass black holes. *A&A*, 614:A14.

Sakurai, Y., Yoshida, N., Fujii, M., S., and Hirano, S. (2017). Formation of intermediate-mass black holes through runaway collisions in the first star clusters. *MNRAS*, 472:1677.

Schleicher, D., Palla, F., Ferrara, A., Galli, D., and Latif, M. (2013). Massive black hole factories: Supermassive and quasi-star formation in primordial halos. *A&A*, 558.

Schneider, R., Omukai, K., Inoue, A., K., and Ferrara, A. (2006). Fragmentation of star-forming clouds enriched with the first dust. *MNRAS*, 369:1437.

Shang, C., Bryan, G. L., and Haiman, Z. (2010). Supermassive black hole formation by direct collapse: keeping protogalactic gas H2 free in dark matter haloes with virial temperatures $T_vir > 10^4 K$. *MNRAS*, 402(2):1249–1262.

Shapiro, S., L. (2005). Spin, accretion, and the cosmological growth of supermassive black holes. *ApJ*, 620:59.

Suazo, M., Prieto, J., Escala, A., and Schleicher, D. (2019). The role of gas fragmentation during the formation of supermassive black holes. *ApJ*.

Sugimura, K., Omukai, K., and Inoue, A., K. (2014). The critical radiation intensity for direct collapse black hole formation: dependence on the radiation spectral shape. *MNRAS*, 445:544.

Toomre, A. (1964). On the gravitational stability of a disk of stars. *The Astrophysical Journal*, 139:1217–1238.

Trac, H., Sills, A., and Pen, U.-L. (2007). A comparison of hydrodynamic techniques for modelling collisions between main-sequence stars. *Monthly Notices of the Royal Astronomical Society*, 377(3):997–1005.

Volonteri, M. (2010). Formation of supermassive black holes. *The Astronomy and Astrophysics Review*, 18(3):279–315.

Wise, J., H., Turk, M., J., and Abel, T. (2008). Resolving the formation of protogalaxies. ii. central gravitational collapse. *ApJ*, 682:745.

Woods, T. E., Agarwal, B., Bromm, V., Bunker, A., Chen, K.-J., Chon, S., Ferrara, A., Glover, S. C. O., Haemmerlé, L., Haiman, Z., and et al. (2018). Titans of the early universe: The prato statement on the origin of the first supermassive black holes. *PASA*, 36.